

Methyl chloride from the Aura Microwave Limb Sounder: First global climatology and assessment of variability in the upper troposphere and stratosphere

M. L. Santee,¹ N. J. Livesey,¹ G. L. Manney,^{2,3} A. Lambert,¹ and W. G. Read¹

Received 21 May 2013; revised 17 September 2013; accepted 20 October 2013; published 16 December 2013.

[1] Methyl chloride (CH₃Cl) is by far the largest natural carrier of chlorine to the stratosphere. Its importance in stratospheric ozone chemistry is expected to increase in the coming decades as emission controls alter the relative contributions from natural and anthropogenic halogen sources. The Microwave Limb Sounder (MLS) on NASA's Aura satellite provides the first daily global observations of CH₃Cl. Here we quantify the quality of the MLS version 3 CH₃Cl data (single-profile precision of ±100 pptv; accuracy of 30–45%; vertical and horizontal resolution of 4–5 km and 450–600 km, respectively) and demonstrate their utility for scientific studies over the vertical range from 147 to 4.6 hPa. We exploit the unmatched scope of the 8 year MLS data set to investigate the spatial, seasonal, and interannual variations in the distribution of CH₃Cl in the upper troposphere/lower stratosphere (UTLS). Like carbon monoxide, CH₃Cl is a marker of pollution from biomass burning that can be lofted to the UTLS very rapidly by deep convection. The climatological seasonal cycle in CH₃Cl reflects variability in regional fire activity and other surface sources as well as convection, and anomalous CH₃Cl enhancements in the tropical upper troposphere are linked to specific episodes of intense burning. Methyl chloride is shown to be very useful as a tracer of large-scale dynamical processes, such as diabatic descent inside the stratospheric winter polar vortices, quasi-isentropic cross-tropopause transport associated with the summer monsoon circulations, and effects related to the quasi-biennial oscillation and the tropical “tape recorder”.

Citation: Santee, M. L., N. J. Livesey, G. L. Manney, A. Lambert, and W. G. Read (2013), Methyl chloride from the Aura Microwave Limb Sounder: First global climatology and assessment of variability in the upper troposphere and stratosphere, *J. Geophys. Res. Atmos.*, 118, 13,532–13,560, doi:10.1002/2013JD020235.

1. Introduction

[2] Methyl chloride (chloromethane, CH₃Cl) is the most abundant chlorine-containing gas in the troposphere [e.g., Graedel and Keene, 1995; Khalil et al., 1999] and is by far the largest natural source of stratospheric chlorine [e.g., Cicerone et al., 1975; Penkett et al., 1980; Khalil et al., 1999; Keene et al., 1999]. In contrast to most other relatively long-lived ozone-depleting gases, CH₃Cl has both natural and anthropogenic sources, although known emissions are predominantly natural in origin [e.g., Keene et al., 1999; World Meteorological Organization, 2011]. It was

first detected in the atmosphere in the mid-1970s [Lovelock, 1975; Grimsrud and Rasmussen, 1975], shortly after which its contribution to the stratospheric chlorine burden was found to have been surpassed by that from manufactured compounds [Cronn et al., 1977; Penkett et al., 1980; Fabian et al., 1981]. Nevertheless, CH₃Cl was estimated to contribute 16% of the stratospheric total inorganic chlorine budget in 2000 [Schauffler et al., 2003]; thus, it continues to account for a significant fraction of chlorine-catalyzed ozone destruction. Methyl chloride will likely regain its predominance as a source of stratospheric chlorine in the coming decades as anthropogenic halocarbons decline in response to regulations mandated by the Montreal Protocol [Montzka et al., 1996; World Meteorological Organization, 2007].

[3] Historically, a substantial imbalance in the global atmospheric CH₃Cl budget has existed, with established sinks far exceeding confirmed sources [e.g., Khalil and Rasmussen, 1999; Butler, 2000; Lee-Taylor et al., 2001; Yoshida et al., 2004, 2006; Xiao et al., 2010]. The latest studies, however, suggest that the gap is narrowing [World Meteorological Organization, 2011]. The bulk of atmospheric CH₃Cl originates from biogenic production by/in vegetation, particularly in the tropics and subtropics [e.g.,

¹Jet Propulsion Laboratory, California Institute of Technology, Pasadena, California, USA.

²NorthWest Research Associates, Socorro, New Mexico, USA.

³Also at Department of Physics, New Mexico Institute of Mining and Technology, Socorro, New Mexico, USA.

Corresponding author: M. L. Santee, Jet Propulsion Laboratory, Mail Stop 233–200, 4800 Oak Grove Drive, Pasadena, CA 91109, USA. (Michelle.L.Santee@jpl.nasa.gov)

Yokouchi et al., 2000, 2002; Rhew et al., 2001; Saito et al., 2008; Blei et al., 2010]. A recent three-dimensional inverse modeling study constrained by observations from surface networks estimated that tropical plants account for 54% of total global CH₃Cl emissions [Xiao et al., 2010]. The second largest contributor to CH₃Cl emissions is biofuel and biomass burning (in particular from smoldering combustion) [e.g., Crutzen et al., 1979; Crutzen and Andreae, 1990; Andreae et al., 1996; Lobert et al., 1999; Andreae and Merlet, 2001], recently confirmed to account for nearly 25% of the CH₃Cl global source strength [Xiao et al., 2010]. Warm tropical and subtropical open ocean and coastal waters, once thought to be the dominant source [e.g., Singh et al., 1983], are now estimated to contribute ~11% to the global CH₃Cl budget [e.g., Moore et al., 1996; Khalil et al., 1999; Hu et al., 2010; Xiao et al., 2010]. Other minor sources include freshwater wetlands, peatbogs, coastal salt marshes, and mangroves [e.g., Varner et al., 1999; Rhew et al., 2000; Rhew and Mazéas, 2010; Dimmer et al., 2001; Manley et al., 2007; Hardacre et al., 2009]; flooded rice paddies [Redeker et al., 2000; Redeker and Cicerone, 2004]; wood-rotting fungi [Harper, 1985; Watling and Harper, 1998; Moore et al., 2005]; and fungus gardens cultivated by leaf cutter ants [Mead et al., 2008]. Atmospheric CH₃Cl also arises through abiotic release from senescent and dead plant material and organic matter in soils and sediments (again primarily in tropical and subtropical regions) [e.g., Keppler et al., 2000, 2005; Hamilton et al., 2003]. Although substantially elevated abundances of CH₃Cl have been measured in the troposphere and stratosphere following major volcanic eruptions [e.g., Rasmussen et al., 1980; Inn et al., 1981; Cronn and Nutmagul, 1982], direct volcanic emissions of CH₃Cl have been estimated to be negligible [Gerlach, 1980; Symonds et al., 1988], with the observed fluxes attributed to the pyrolytic combustion of vegetation and organic debris associated with lava or pyroclastic flows. Exclusively anthropogenic activities such as coal combustion, municipal and domestic waste incineration, and industrial processes, mainly concentrated in the Northern Hemisphere, make minor contributions (~4%) to the atmospheric flux of CH₃Cl [Graedel and Keene, 1995; McCulloch et al., 1999; Xiao et al., 2010]. Although released at the surface, CH₃Cl is transported to the middle atmosphere through dynamical processes both fast (e.g., convection) and slow (e.g., large-scale ascent).

[4] The main loss mechanism for CH₃Cl is oxidation by the hydroxyl radical (OH) in the troposphere [e.g., Cicerone et al., 1975; Crutzen and Gidel, 1983; Graedel and Keene, 1995]. The CH₃Cl lifetime with respect to reaction with tropospheric OH is 1.5 years [World Meteorological Organization, 2011]. In the tropical tropopause layer, a distinct region with both tropospheric and stratospheric characteristics, the lifetime of CH₃Cl has been estimated to be ~12 years based on the rate of reaction with OH [Marcy et al., 2007]. Another significant CH₃Cl sink is chemical and biological degradation in the cold waters of the middle- and high-latitude oceans [e.g., Tait et al., 1994; Moore et al., 1996; Tokarczyk et al., 2003a, 2003b; Yvon-Lewis et al., 2004], with the partial atmospheric lifetime of CH₃Cl with respect to irreversible oceanic uptake recently estimated to be ~12 years [Hu et al., 2013]. Minor tropospheric sinks include consumption by anaerobic and aerobic micro-

bial processes in soils [e.g., Khalil and Rasmussen, 2000; McAnulla et al., 2001; Rhew et al., 2003, 2007; Keppler et al., 2005] and reactions with atomic chlorine in the marine boundary layer (particularly in the tropics) [Khalil and Rasmussen, 1999; Keene et al., 1999]. Photolysis of CH₃Cl is insignificant in the troposphere and lowermost stratosphere [Lee-Taylor et al., 2001; Marcy et al., 2007], and loss of CH₃Cl to the stratosphere constitutes only a small fraction of the tropospheric removal [Keene et al., 1999; Yoshida et al., 2004]. The major CH₃Cl destruction mechanisms in the stratosphere are photolysis, which represents ~30–40% of the total loss, and reaction with OH (and to a lesser extent O(¹D)), leading to a global mean lifetime against strictly stratospheric removal processes of ~35–60 years [Avallone and Prather, 1997; Weisenstein et al., 1992]. Collectively, all of these CH₃Cl loss processes lead to an overall global average atmospheric lifetime of 1–1.2 years [World Meteorological Organization, 2011; Hu et al., 2013].

[5] In addition to an increase in its relative proportion of the chlorine budget with the reduction in anthropogenic emissions, several analyses indicate that the stratospheric burden of CH₃Cl may have grown slightly over the last ~10–100 years [Butler et al., 1999; Aydin et al., 2004; Trudinger et al., 2004; Brown et al., 2011; World Meteorological Organization, 2011], although other studies suggest small decreasing trends at some sites [Khalil and Rasmussen, 1999; Kaspers et al., 2004; Simmonds et al., 2004]. Changes in the atmospheric oxidative capacity may appreciably alter tropospheric CH₃Cl abundances and thus ultimately the amount of chlorine in the stratosphere [e.g., Crutzen and Gidel, 1983]. Furthermore, because climate variability strongly influences the frequency and severity of wildfires [e.g., Westerling et al., 2006; Scholze et al., 2006], larger pyrogenic CH₃Cl emissions can be expected in the future. Similarly, since CH₃Cl fluxes from/to many natural sources/sinks (including both biogenic and abiotic processes) vary depending on ambient environmental conditions (e.g., temperature, moisture/humidity, salinity, acidity, the types of organic material present, and the length of the growing season), changes in global climate and land use patterns may also have a substantial impact on the CH₃Cl input to and uptake from the atmosphere, and thus the stratospheric chlorine loading. Indeed, measurements of CH₃Cl in air extracted from polar firn (unconsolidated snow) and ice core samples indicate significant long- and short-term fluctuations and trends that may be linked to variations in biomass burning or global mean temperature [Aydin et al., 2004; Trudinger et al., 2004; Williams et al., 2007]. Strong pulses from unusually large or intense fire events have been shown to perturb the global CH₃Cl burden, and relaxation back to equilibrium following such anomalous emissions has been proposed to explain intervals of downward CH₃Cl trends at some sites [e.g., Simmonds et al., 2004; Trudinger et al., 2004]. Evidence for a positive linear CH₃Cl temperature response suggests that, in a future warmer climate, increases in CH₃Cl could offset some of the projected decline in anthropogenic chlorine and delay stratospheric ozone recovery [Williams et al., 2007]. For all of these reasons, a quantitative understanding of the distribution of stratospheric CH₃Cl will be valuable in enhancing our predictive capability for stratospheric chlorine chemistry and ozone layer stability.

Table 1. Summary of Aura MLS v3.3 Characteristics for Selected Species in the UTLS

Species	Resolution		Systematic Uncertainty (%)
	Vertical × Horizontal ^a (km)	Precision ^b	
CO	4.5–5.5 × 350–700	±15–20 ppbv	30
H ₂ O	2.5–3.5 × 200–300	±5–20%	5–20
N ₂ O	4–6 × 350–600	±15–25 ppbv	10–25
O ₃	2.5–3 × 350–500	±0.02–0.1 ppmv	5–20

^aHorizontal resolution in the direction along the measurement track.

^bPrecision on individual profiles, expressed in terms of mixing ratio except for water vapor, which is retrieved as the logarithm of the mixing ratio and thus has precision expressed as a percentage.

[6] Previously, limited observations of CH₃Cl were obtained in the upper troposphere/lower stratosphere (UTLS) through in situ and remote techniques from balloons and aircraft [e.g., *Blake et al.*, 1996, 1997, 2001, 2003; *Cronn et al.*, 1977; *Fabian et al.*, 1981, 1996; *Marcy et al.*, 2007; *Penkett et al.*, 1980; *Pierotti et al.*, 1980; *Schauffler et al.*, 1993, 2003; *Fischer et al.*, 2002; *Scheeren et al.*, 2002, 2003; *Schmidt et al.*, 1985; *Sen et al.*, 1999; *Singh et al.*, 2003]. Stratospheric profiles of CH₃Cl have also been measured from space using infrared solar occultation by the Atmospheric Trace Molecule Spectroscopy Spacelab 3 and space shuttle missions [*Park et al.*, 1986; *Zander et al.*, 1992, 1996]. More recently, the Atmospheric Chemistry Experiment Fourier Transform Spectrometer (ACE-FTS) on the Canadian SCISAT-1 satellite has provided a multiyear CH₃Cl data set [e.g., *Nassar et al.*, 2006; *Brown et al.*, 2011]. Although ACE-FTS affords much better coverage than ground-based, balloon, or aircraft instruments, solar occultation techniques provide only a small number of measurements per day around a circle of latitude in each hemisphere. Moreover, a given latitude zone may frequently go unmeasured by ACE-FTS for periods of a month or longer [e.g., *Nassar et al.*, 2006], especially in the tropics (of particular interest for CH₃Cl). In fact, ACE-FTS averages fewer than 300 occultations per year in the latitude band between 30°S and 30°N [*Brown et al.*, 2011], typically sampling this region only during 4–5 months of the year at intermittent intervals.

[7] With the release of the version 3 data processing algorithms [*Livesey et al.*, 2013b], the Aura Microwave Limb Sounder (MLS) now provides measurements of CH₃Cl in the uppermost troposphere and the stratosphere. These daily global measurements from Aura MLS, which at the time of writing have been obtained over more than eight complete annual cycles, represent by far the most comprehensive CH₃Cl observational record. The unprecedented scope of the Aura MLS data set makes it uniquely suited to characterizing spatial, seasonal, and interannual variations in the distribution of CH₃Cl in the tropopause region and the stratosphere, providing a baseline against which the future stratospheric CH₃Cl burden may be assessed. After a brief description of the Aura MLS measurements and meteorological analyses used in this work (section 2), we summarize the results of various validation exercises to quantify the quality of the MLS CH₃Cl data (section 3). We then present the first global climatology of CH₃Cl in the UTLS and compare the behavior of CH₃Cl to that observed in other species measured by MLS (section 4). The intent of this paper is to introduce

the new Aura MLS CH₃Cl data set and demonstrate its usefulness for in-depth analysis.

2. Measurement Description

[8] MLS measures millimeter- and submillimeter-wavelength thermal emission from the limb of Earth's atmosphere [*Waters et al.*, 2006]. The Aura MLS fields of view point in the direction of orbital motion and vertically scan the limb in the orbit plane, leading to data coverage from 82°S to 82°N latitude on every orbit. Because the Aura orbit is sun-synchronous (with a 13:45 local time ascending equator-crossing time), MLS observations at given latitudes on either the ascending (mainly day) or descending (mainly night) portions of the orbit have approximately the same local solar time.

[9] In addition to CH₃Cl, this study uses a suite of version 3.3 (v3.3) MLS measurements, including ozone (O₃), water vapor (H₂O), nitrous oxide (N₂O), and carbon monoxide (CO). A detailed description of the previous version of MLS data, v2.2, and information on its quality can be found in dedicated validation papers by *Livesey et al.* [2008a] and *Froidevaux et al.* [2008] for upper tropospheric and stratospheric O₃, respectively; *Read et al.* [2007] and *Lambert et al.* [2007] for upper tropospheric and stratospheric H₂O, respectively; *Lambert et al.* [2007] for stratospheric N₂O; and *Livesey et al.* [2008a] and *Pumphrey et al.* [2007] for upper tropospheric and stratospheric CO, respectively. The v3.3 Aura MLS data processing algorithms have led to notable refinements in several products. The precision, resolution, and useful vertical range of the v3.3 measurements, as well as assessments of their accuracy through comparisons with correlative data sets, are reported for each species in the v3.3 Level 2 data quality and description document [*Livesey et al.*, 2013b]. Table 1 briefly summarizes the quality of the relevant v3.3 MLS data (excluding CH₃Cl) at the upper tropospheric and stratospheric levels shown here.

[10] One particularly noteworthy improvement in v3.3 MLS data is mitigation of the substantial (~0.1–0.4 ppbv) latitudinally varying negative bias present in the v2.2 (and earlier) chlorine monoxide (ClO) values at retrieval levels below (i.e., pressures larger than) 22 hPa. *Santee et al.* [2008] suggested that contamination from an interfering species such as CH₃Cl, which has lines in two wing channels of the 640 GHz band used to measure ClO, may have been partially responsible for the ClO bias; they showed results from precursory v3 algorithms in which CH₃Cl was also retrieved that demonstrated significant reduction in the bias in lower stratospheric ClO. Further refinements in the algorithms yielded not only an improved ClO product [*Livesey et al.*, 2013b] but also a reliable retrieval of CH₃Cl. An assessment of the quality, resolution, and useful vertical range of the v3.3 MLS CH₃Cl data set is provided in the following section.

[11] In addition to MLS measurements, we make extensive use of meteorological data from the NASA Global Modeling and Assimilation Office Goddard Earth Observing System Versions 5.1.0 and 5.2.0 (GEOS-5) analyses. Along with standard meteorological variables, GEOS-5 products include an expansive set of fields from the model and assimilation system, including potential vorticity (PV) calculated

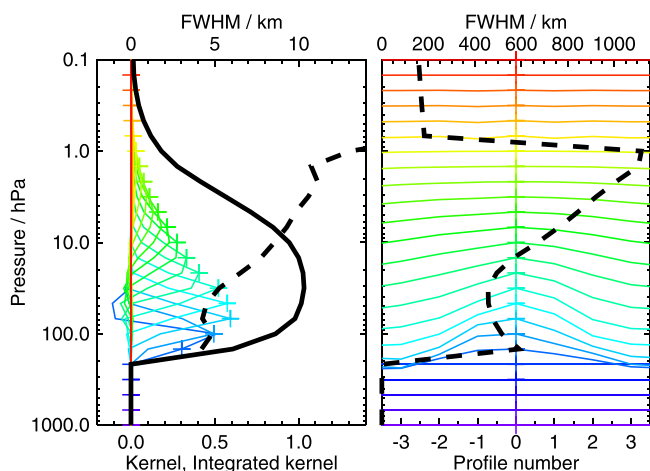


Figure 1. Two-dimensional (vertical and horizontal along-track) averaging kernels for the MLS version 3.3 (v3.3) CH₃Cl data at the equator; variation in the averaging kernels is sufficiently small that these are representative of typical profiles. Colored lines show the averaging kernels as a function of MLS retrieval level, indicating the region of the atmosphere from which information is contributing to the measurements on the individual retrieval surfaces, which are denoted by plus signs in corresponding colors. The dashed black line indicates the resolution, determined from the full width at half maximum (FWHM) of the rows of the averaging kernel matrix, approximately scaled into kilometers (top axes). (left) Vertical averaging kernels (integrated in the horizontal dimension for five along-track profiles) and resolution. The solid black line shows the integrated area under each kernel (horizontally and vertically). (right) Horizontal averaging kernels (integrated in the vertical dimension) and resolution. The horizontal averaging kernels are shown scaled in the vertical direction such that a unit averaging kernel amplitude is equivalent to a factor of 10 change in pressure.

internally in the model. For most of the work presented here, we use the Modern-Era Retrospective Analysis for Research and Applications (MERRA) 32 year reanalysis [Rienecker *et al.*, 2011]. However, unlike the other fields, MERRA PV is produced on pressure levels on a reduced resolution grid, rather than on model levels on the full resolution grid. Therefore, analyses from the operational near real-time (NRT) system [Rienecker *et al.*, 2008] are used for all PV overlays on figures. On the other hand, MERRA PV is used in the calculation of effective diffusivity (discussed further in section 4), for which a smoother PV field on a coarser grid is advantageous. Throughout this paper, absolute values are used whenever PV is specified.

3. Validation of the Aura MLS v3.3 CH₃Cl Measurements

3.1. Resolution and Precision

[12] The MLS retrieval algorithms employ a two-dimensional approach that accounts for the fact that the radiances for each limb scan are influenced by the state of

the atmosphere at adjacent scans along the forward-looking instrument line of sight [Livesey *et al.*, 2006]. The resolution of the retrieved data can be described using “averaging kernels” [e.g., Rodgers, 2000]; the two-dimensional nature of the MLS data processing system means that the kernels describe both vertical and horizontal resolution (Figure 1). Values of the integrated kernel near unity indicate that the majority of information for that level has come from the measurements themselves and not the a priori; Figure 1 shows that the measurements dominate at pressures greater than 3.2 hPa, above which level the integrated kernel drops below 0.5. Smoothing, imposed on the retrieval system in both the vertical and horizontal directions to enhance retrieval stability and precision, degrades the inherent resolution of the measurements. Thus, although CH₃Cl measurements are reported at six pressure levels per decade change in pressure (spacing of ~ 2.7 km), their vertical resolution as determined from the full width at half maximum of the averaging kernels is ~ 4 – 6 km in most of the lower stratosphere, degrading to 7–10 km at and above (i.e., at pressures less than) 15 hPa (Figure 1). Because the MLS composition retrievals are performed on a fixed pressure grid and the pressure at the tangent point of the limb ray is retrieved for each measurement point in the vertical limb scan [Livesey *et al.*, 2006], there is no ambiguity in the pressure registration of the MLS observations. In addition, the averaging kernels are fairly symmetric, and for the most part they peak at their nominal position. However, overlap in the averaging kernels for the 100 and 147 hPa retrieval surfaces indicates that the 147 hPa retrieval does not provide as much independent information as is given by retrievals at higher altitudes.

[13] As shown in Figure 1, the MLS averaging kernels are fairly “sharp” functions, and their relative sharpness enables realistic depiction of atmospheric structure on length scales somewhat finer than suggested by the averaging kernel widths. Although MLS measurements have previously been shown to accurately characterize the large-scale morphology of several trace gases in the UTLS [e.g., Livesey *et al.*, 2008b; Santee *et al.*, 2007], their ability to discriminate features of small vertical scale has only recently been explored in detail. Manney *et al.* [2009b, 2011] and Santee *et al.* [2011] demonstrated that, despite their nominal vertical resolution in the UTLS (2.5–4.5 km, depending on the species), MLS data successfully represent distinct, relatively localized vertical structure in trace gas distributions in this region. The results presented in subsequent sections of this paper confirm that atmospheric features with height scales shorter than the formal vertical resolution derived from the averaging kernels are captured in MLS CH₃Cl data, albeit in a spatially smoothed manner.

[14] From the horizontal averaging kernels (Figure 1), the along-track horizontal resolution is determined to be ~ 600 km at 147 hPa, ~ 450 – 500 km from 100 to 22 hPa, and ~ 550 – 850 km at and above 15 hPa. The cross-track field-of-view width of the 640 GHz radiometer is ~ 3 km. The along-track separation between adjacent retrieved profiles is 1.5° great circle angle (~ 165 km), whereas the longitudinal separation of MLS measurements, set by the Aura orbit, is 10° – 20° over low and middle latitudes, with much finer sampling in the polar regions (up to the poleward limit of MLS coverage at 82°).

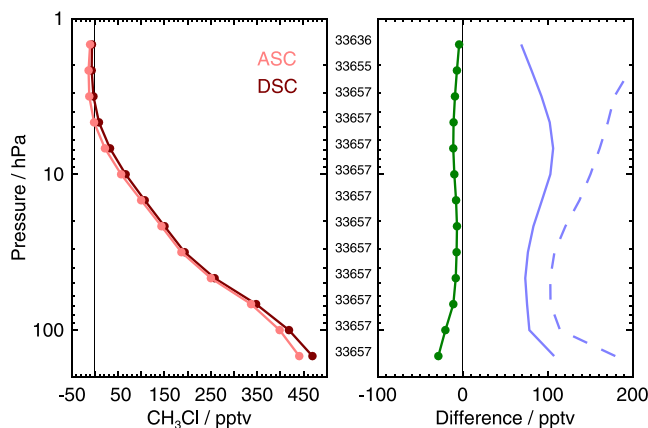


Figure 2. (left) Ensemble mean profiles for ascending (light red) and descending (dark red) orbit matching pairs of MLS v3.3 CH₃Cl profiles averaged over a representative year of data (2005). Symbols indicate MLS retrieval pressure levels. (right) Mean differences (ascending–descending) in pptv (green solid line). Also shown are the standard deviations about the mean differences (light blue solid line) and the root sum square (RSS) of the precisions calculated by the retrieval algorithm for the two sets of profiles (light blue dashed line). The observed scatter about the mean differences and the reported precision values have been scaled by $1/\sqrt{2}$ (to convert from standard deviations of differences into standard deviations of individual data points); hence, the light blue solid line represents the statistical repeatability of the MLS measurements, and the light blue dashed line represents the expected 1σ precision for a single profile. The thin black lines mark zero in each panel. The number of crossing pairs of measurements being compared at each pressure level is noted in the space between the panels.

[15] The precision of the MLS CH₃Cl data is estimated empirically by comparing profiles measured at the intersections of ascending (day) and descending (night) portions of the orbit [e.g., Lambert *et al.*, 2007]. Under ideal conditions (i.e., a quiescent atmosphere), the standard deviation about the mean differences between such matched profile pairs provides a measure of the precision of the individual data points. In practice, however, real changes in the atmosphere may occur over the 12 h interval between the intersecting measurement points, in which case the observed scatter provides an upper limit on the estimate of precision, assuming that the a priori has a negligible influence on the retrieval (a reasonable assumption at least at pressures greater than 3.2 hPa). The precision estimates were found to be essentially invariant with time; results for a representative year of data are shown in Figure 2. The observed standard deviation values are ~ 100 pptv or less throughout the vertical domain. Mean differences between paired crossing profiles are ~ 10 pptv or less except at the lowest two levels, where they reach 20–30 pptv. Given the large number of data points being compared (almost 34,000), these ascending–descending differences are substantially larger than the standard error of the mean, implying the presence of significant systematic biases. These biases likely arise from the cumulative effect of various factors in the retrieval

system that can vary diurnally or along the orbit, such as interferences (e.g., H₂O and ClO), or thermal emissions from the MLS antenna. Analyses performed separately on sets of ascending-only and descending-only measurements suggest that, although significant, these biases have little or no impact on the scientific conclusions drawn in this study, and throughout the rest of the paper, data from both sides of the orbit are shown together.

[16] The precision reported for each data point by the Level 2 data processing system exceeds the observationally determined precision throughout the vertical range (Figure 2), indicating that the smoothing (regularization) applied to stabilize the retrieval system and improve the precision has a non-negligible influence. Because the reported precisions take into account occasional variations in instrument performance, the best estimate of the precision of an individual data point is the value quoted for that point in the Level 2 Geophysical Product (L2GP) files, but it should be borne in mind that this approach slightly overestimates the actual measurement noise. Note that the estimates reported here represent the precisions at each pressure level of a single profile; precision can generally be improved by averaging, with the precision of an average of N profiles being $1/\sqrt{N}$ times the precision of an individual profile (although the actual standard error of the mean can in some cases be even smaller [Toohey and von Clarmann, 2013]). For the averaged quantities shown in subsequent sections, the estimated precisions are smaller than the single-profile value by at least a factor of 10, and considerably more in some cases.

3.2. Quantification of Systematic Uncertainty

[17] Systematic uncertainties arise from a variety of sources, including instrumental issues (e.g., radiometric calibration, field of view characterization), spectroscopic uncertainty, and approximations in the forward model and retrieval formulation or implementation. Here we summarize the relevant results of a comprehensive quantification of these uncertainties for CH₃Cl that was performed as part of the validation of the v3.3 MLS products. A similar approach was previously undertaken for the assessment of systematic errors in the MLS v2.2 data set (for details, see Read *et al.* [2007], Appendix A).

[18] Sets of modeled errors reflecting the potential magnitude of several sources of uncertainty are applied to simulated MLS cloud-free (and noise-free) radiances, calculated based on a model atmosphere for an entire day of MLS observations (nearly 3500 profiles). The modeled perturbations correspond to either 2σ estimates of the uncertainties in the relevant parameters, or an estimate of their maximum reasonable errors based on instrument knowledge and/or design requirements. The sets of perturbed radiances are then run through the routine MLS data processing algorithms. Differences between these runs and results from an unperturbed retrieval quantify the systematic uncertainty arising from each parameter.

[19] Although the term “systematic uncertainty” is often associated with consistent additive biases and/or scaling errors, many sources of systematic uncertainty in the MLS measurement system give rise to additional scatter in the retrieved values. For example, although an error in the spectroscopy of a given species induces a bias in that product, it

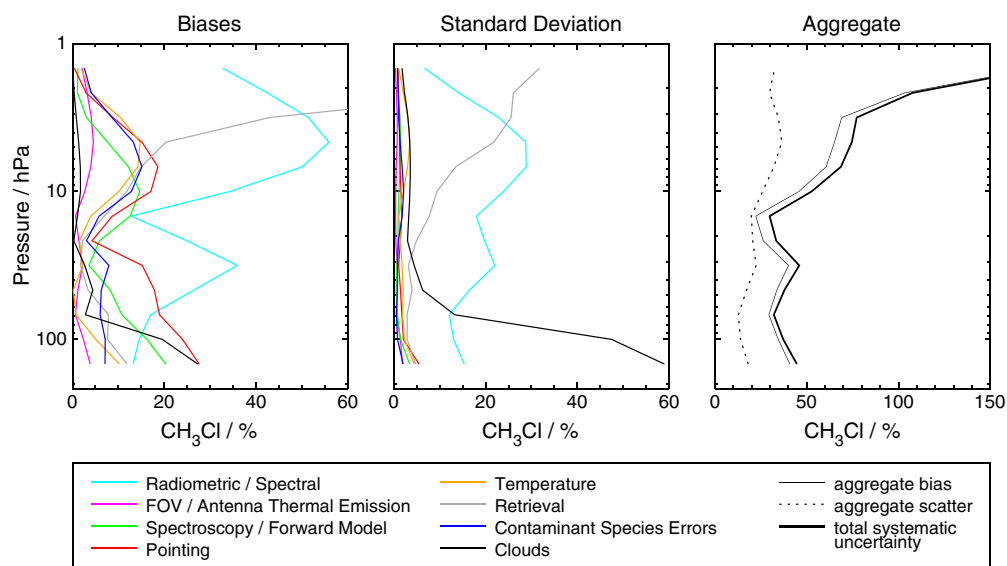


Figure 3. The estimated impact of various families of systematic uncertainty on the MLS v3.3 CH₃Cl observations. (left, middle) The possible biases and additional scatter introduced by the various error families. Colored lines denote the estimated contributions from uncertainties in the following: MLS radiometric and spectral calibration (cyan), the MLS field of view shape and antenna transmission efficiency (magenta), spectroscopic databases and forward model approximations (green), pointing (red), the MLS temperature product (gold), and other MLS products (blue). Errors arising from approximations in the retrieval formulation are shown in grey, and the typical impact of cloud contamination is depicted by the black line. (right) The RSS of all the possible biases (thin solid line), all the additional scatter terms (thin dotted line), and the RSS sum of the two (thick solid line), excluding the effects of clouds.

can affect the retrievals of other species with weaker signals in a manner that is dependent on its atmospheric abundance and morphology. By applying the same systematic error from each source to a full day’s worth of measurements encompassing the global CH₃Cl distribution, we obtain an ensemble of uncertainty estimates. This approach allows the bias and scatter in individual differences from the unperturbed control run to be quantified separately, enabling the extent to which such errors will be reduced through averaging to be estimated to first order.

[20] Differences between the retrieved product from the unperturbed run and the original model atmosphere (the “truth”) provide a measure of uncertainties attributable to retrieval formulation and numerics. To test the sensitivity of the retrieved mixing ratios to the a priori information, another retrieval of the unperturbed radiances is performed with the a priori increased by a factor of 1.5. Other (typically smaller) uncertainty sources are quantified through analytic calculations based on simplified models of the MLS measurement system [Read *et al.*, 2007].

[21] Figure 3 summarizes the results of the uncertainty characterization for the MLS v3.3 CH₃Cl measurements. The largest potential source of both bias and scatter throughout much of the profile is the spectral distortion induced in calibrated MLS radiances by receiver nonlinearities (cyan). Pointing uncertainties (red), which arise from uncertainty in the width of the O₂ lines used to determine limb tangent pressure and in the vertical offsets between the fields of view of the MLS 118 and 640 GHz receivers, dominate at the lowest retrieval levels. Uncertainty in the dry air continuum emission/absorption (green) and retrieval numerics (grey) also produce significant biases. Most other potential

uncertainty sources, such as errors in the MLS temperature product (gold), contaminating species (blue), or the combined effects of uncertainty in the MLS field of view shape and the thermal sensitivity of the antenna (magenta), are found to have relatively modest impact, with the exception of clouds.

[22] Although MLS observations are unaffected by thin cirrus clouds or stratospheric aerosols, thick clouds associated with deep convection can influence the MLS radiances. The contribution of clouds to the systematic uncertainty has been quantified by adding the effects of scattering from a representative cloud field to the simulated radiances and then comparing retrievals based on these radiances to the unperturbed results. The cloud-induced effects shown in Figure 3 are estimated by considering only the cloudy profiles (as defined by the known amount of cloud in the “truth” field). This analysis indicates that the presence of thick clouds (black) can potentially induce substantial biases in the CH₃Cl at the bottom two retrieval levels; the variability that clouds introduce into the retrievals at those levels is even larger, dwarfing that from all other sources.

[23] Because some errors may be correlated and thus may compensate or amplify one another, we represent the aggregate bias and scatter as the root sum square (RSS) of the respective biases and scatters contributed by the various parameters investigated in these experiments. The modeled sources of systematic uncertainty (excluding clouds, since in principle they can be detected and the affected profiles removed) are estimated to introduce cumulative biases of up to 45% and additional scatter of up to 25% at and below (i.e., at pressures greater than) 10 hPa. The total systematic uncertainty, calculated by combining (RSS) the contributions from

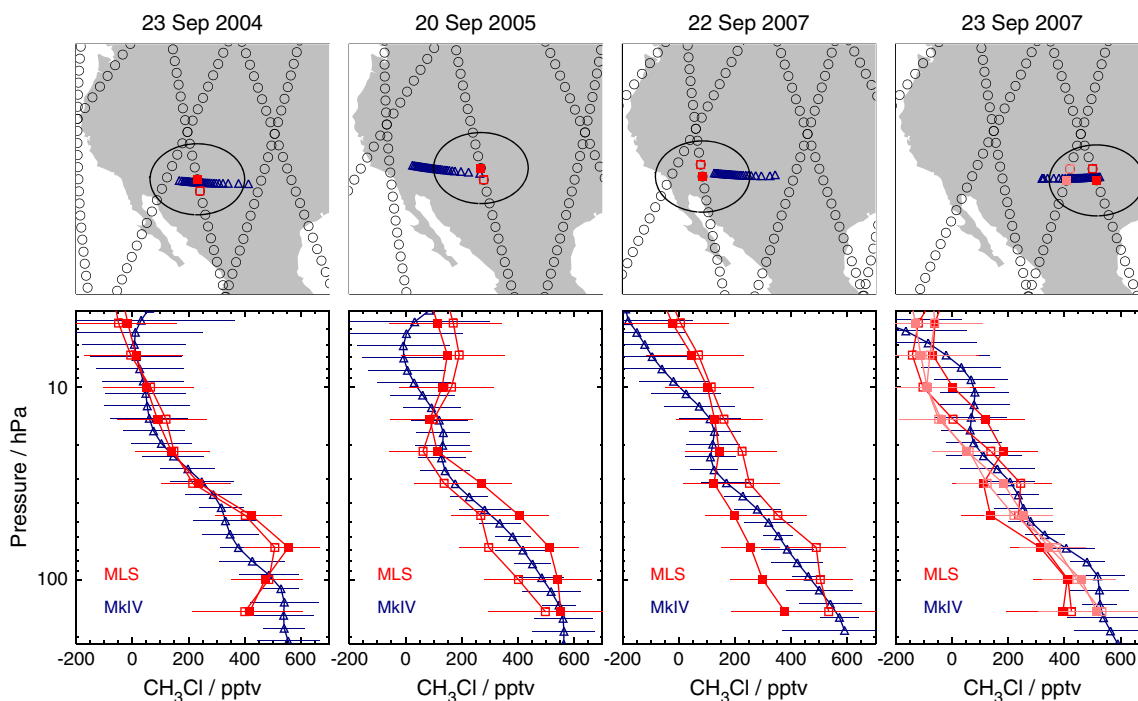


Figure 4. (top) Tangent point locations of the limb path of the balloon-borne MkIV instrument (blue triangles) during flights from Fort Sumner, NM in September 2004, 2005, and 2007. Measurement tracks from nearby MLS orbits are also shown (open circles). The two MLS data points closest to the balloon measurements geographically and temporally are indicated by red squares, with the closer one denoted by a filled symbol; for the 23 September 2007 flight, a second set of MLS profiles is also highlighted (light red). The 500 km radius around the closest MLS point is overlaid in black. (bottom) Profiles of CH₃Cl from MLS and MkIV, corresponding to the colored symbols in Figure 4 (top). Error bars represent the estimated precisions of each instrument, taken from the data files.

both the bias and the scatter terms, is approximately 30–45% in the UTLS.

3.3. Recommended Vertical Range

[24] Although CH₃Cl is retrieved over the range 147 to 0.001 hPa, because of the degradation in resolution and expected precision, the reduction in independent information contributed by the measurements, and the results of simulations using synthetic data as input radiances to test the closure of the retrieval system, the data are not deemed reliable at retrieval pressures less than 4.6 hPa. Despite the overlap in the averaging kernels for the 147 and 100 hPa surfaces discussed above, the simulations show that the retrieved CH₃Cl values track the variations in the “truth” field at both levels. Moreover, the retrievals (of real data) at 147 hPa display significant features not seen at 100 hPa (not shown) that are believed to represent actual atmospheric variations. Thus, we recommend that the v3.3 CH₃Cl data may be used for scientific studies between 147 and 4.6 hPa (inclusive), although the reduced sensitivity at the extremes of this range, as well as the relatively coarse vertical resolution of the retrieved profiles, should be borne in mind.

3.4. CH₃Cl Data Usage Guidelines

[25] In addition to the data values, the CH₃Cl L2GP files contain corresponding estimated precision fields and other diagnostics of data quality (for more detailed information about these quantities, see *Livesey et al.* [2013b]). The

reported precision values are flagged negative where the a priori information has had a strong influence on the retrieval (indicating reduced measurement sensitivity); thus only data points for which the associated precision in the L2GP file is a positive number should be used in scientific analyses.

[26] Three additional data quality metrics are provided for every vertical profile. The “Status” bit field is used to report operational abnormalities or problems with the retrievals; odd values of Status signify that the profile should not be used. Nonzero but even values of Status indicate that the profile has been marked as questionable, usually because the measurements may have been affected by the presence of thick clouds. Globally, fewer than ~1–2% of CH₃Cl profiles are typically identified in this manner, but this value rises to ~3–5% in the tropics on a typical day. Cloud artifacts may be especially prevalent in the data at the 147 hPa retrieval level. For simplicity, we recommend that all profiles with nonzero values of Status be discarded. Note, however, that rejecting in their entirety all profiles with nonzero Status may be unnecessarily severe at and above (i.e., at pressures equal to or smaller than) 46 hPa, where clouds have negligible impact; thus, otherwise good-quality profiles with nonzero but even Status values may be used without restriction at those levels as long as they are removed at larger pressures.

[27] The “Quality” field describes how well the measured MLS radiances have been fitted by the Level 2 algorithms. Only CH₃Cl profiles with a value of Quality greater than 1.3

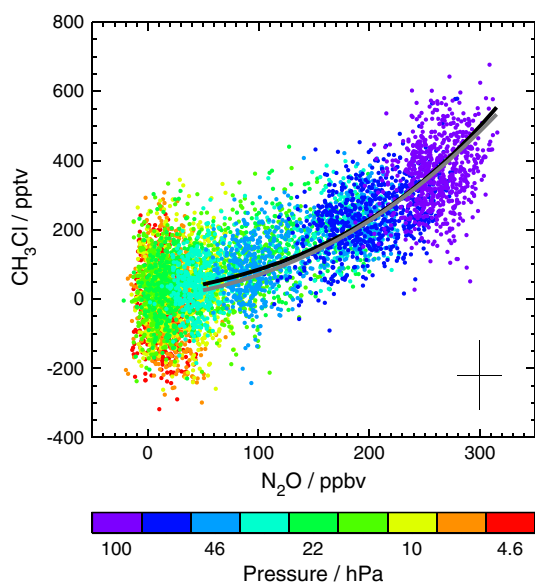


Figure 5. MLS CH₃Cl versus N₂O for 1 February 2008 (dots), color coded by retrieval pressure level. Overlaid in black is the CH₃Cl/N₂O correlation curve calculated from a polynomial equation derived from in situ measurements taken over the period January–March 2000 during the SOLVE campaign (valid for values of N₂O from 50 to 315 ppbv) [Schauffler *et al.*, 2003]. A similar fit to the MLS measurements on this date is indicated by the grey curve. Because SOLVE whole air samples were collected over the latitude range 52°–88°N, only MLS measurements taken poleward of 52°N are shown and used in the fit. The cross in the lower right illustrates the typical precisions of the MLS N₂O and CH₃Cl measurements. Changes in N₂O abundances over the interval from 2000 to 2008 are neglected in this analysis.

should be used in scientific studies. This threshold typically excludes less than 1% of CH₃Cl profiles on a daily basis; however, it potentially discards some “good” data points while not necessarily identifying all “bad” ones. Additional information on the success of the retrieval is conveyed by the “Convergence” field, which compares the fit achieved for each “chunk” of ~10 profiles to that expected by the retrieval algorithms; values around 1.0 typically indicate full convergence. Only CH₃Cl profiles with a value of Convergence less than 1.05 should be used. On a typical day, this threshold for Convergence discards very few (0.3% or less) of the CH₃Cl profiles, most (but not all) of which are also filtered out by the other quality control measures.

3.5. Comparisons With Correlative Data Sets

[28] As part of the Aura validation program, measurements from the Jet Propulsion Laboratory MkIV solar occultation Fourier Transform infrared spectrometer were obtained near Aura overpasses during balloon campaigns in Fort Sumner, New Mexico (35°N) in September 2004, 2005, and 2007. MkIV measures the 650–5650 cm⁻¹ region with 0.01 cm⁻¹ spectral resolution [Toon, 1991]. Profiles, obtained at sunrise or sunset, have a vertical resolution of 2–3 km. Systematic errors caused by spectroscopic uncertainties are as large as 15% for MkIV stratospheric CH₃Cl profiles [Toon

et al., 1999]. Comparisons between the balloon occultations and coincident (within ±1° of latitude, ±12° of longitude, and ±12 h) MLS measurements are shown in Figure 4. It is difficult to draw definitive conclusions on the basis of so few data points (especially given their limited precision), but the overall shapes of the profiles are generally similar, and agreement within the combined precisions of the two instruments is found throughout the vertical range. In particular, for all coincidences MLS CH₃Cl mixing ratios are very close to or smaller than those from MkIV at the lowest MLS retrieval levels (100 and 147 hPa). These comparisons are consistent with the results of the systematic uncertainty analysis discussed in section 3.2, suggesting an accuracy of 50% or better for the MLS CH₃Cl data.

[29] Aircraft measurements of a large suite of organic chlorine-containing compounds, including CH₃Cl, were obtained during the Stratospheric Aerosol and Gas Experiment III Ozone Loss and Validation Experiment (SOLVE) campaign in January–March 2000 [Schauffler *et al.*, 2003]. The SOLVE CH₃Cl data show a compact correlation with N₂O [Schauffler *et al.*, 2003], as had CH₃Cl from whole air samples obtained during a previous Arctic airborne campaign [Avallone and Prather, 1997]. Tracer-tracer correlation plots provide a means of removing the effects of day-to-day meteorological variations on stratospheric trace gases, allowing intercomparison of noncolocated

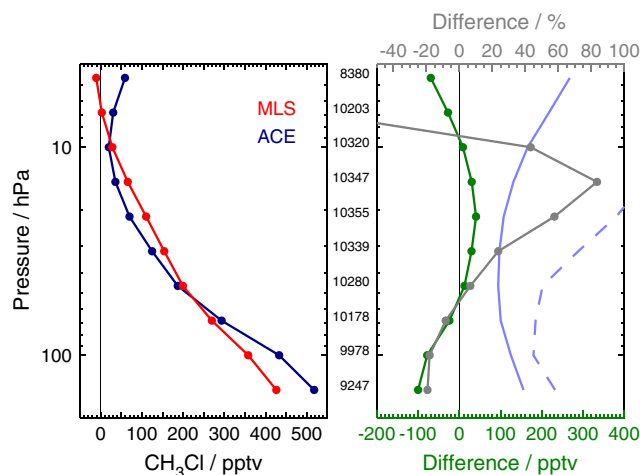


Figure 6. Comparison of coincident (within ±1° in latitude, ±8° in longitude, and ±12 h) v3.3 MLS and v3 ACE-FTS CH₃Cl profiles over a 4 year period (December 2004 to December 2008). The ACE-FTS profiles have been linearly interpolated in log pressure to the fixed MLS retrieval pressure grid for this comparison. (left) Ensemble mean profiles for MLS (red) and ACE-FTS (blue); symbols indicate MLS retrieval pressure levels. (right) Differences (MLS–ACE-FTS) in pptv (green, bottom axis) and percent (grey, top axis), calculated by dividing the mean differences by the mean ACE-FTS value at each pressure level. Also shown are the standard deviation about the mean differences (light blue solid line) and the RSS of the precisions of the two data sets (light blue dashed line). The thin black lines mark zero in each panel. The number of coincident measurements being compared at each pressure level is noted in the space between the panels.

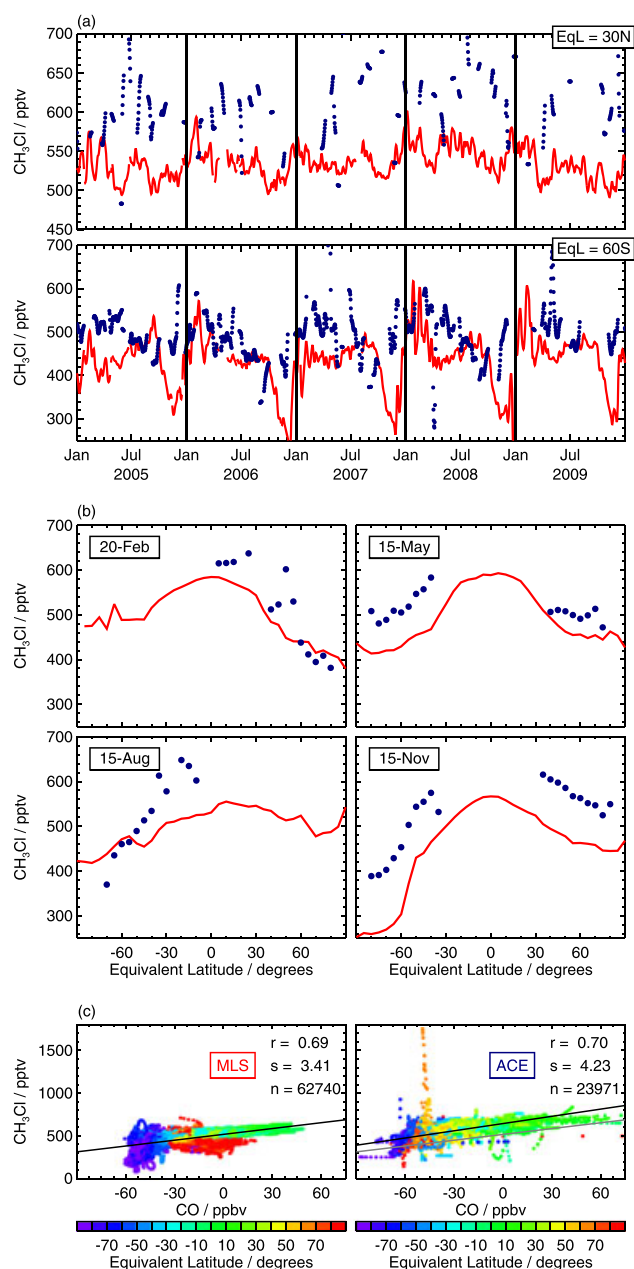


Figure 7. (a) Time series of v3.3 MLS (red) and v3 ACE-FTS (blue) CH₃Cl data, interpolated to the 370 K potential temperature surface using Global Modeling and Assimilation Office Goddard Earth Observing System (GEOS-5) temperatures, for 5° equivalent latitude (EqL) bands centered at 30°N and 60°S. See text for details of the gridding procedure. (b) MLS (red) and ACE-FTS (blue) CH₃Cl data as a function of EqL for a representative day in each season. Gridded data for each date are averaged over the 5 year interval 2005–2009; only latitude bins for which three or more years of measurements are available are plotted. (c) MLS (left) and ACE-FTS (right) CH₃Cl/CO correlations over the entire 5 year period, color coded by EqL. The correlation coefficient (r), slope of the fitted line (s , in pptv/ppbv), and number of points in the gridded fields (n) are shown in each panel. The black line depicts the fit to the data for that instrument; the grey line on the ACE-FTS panel shows the MLS fit for comparison.

measurements. Figure 5 compares the correlation derived from SOLVE data to that obtained from a representative day of MLS observations in the same season. Although characterized by a greater degree of scatter due to measurement noise, the MLS data (colored points) display essentially the same CH₃Cl/N₂O relationship as the in situ measurements (compare black and grey curves).

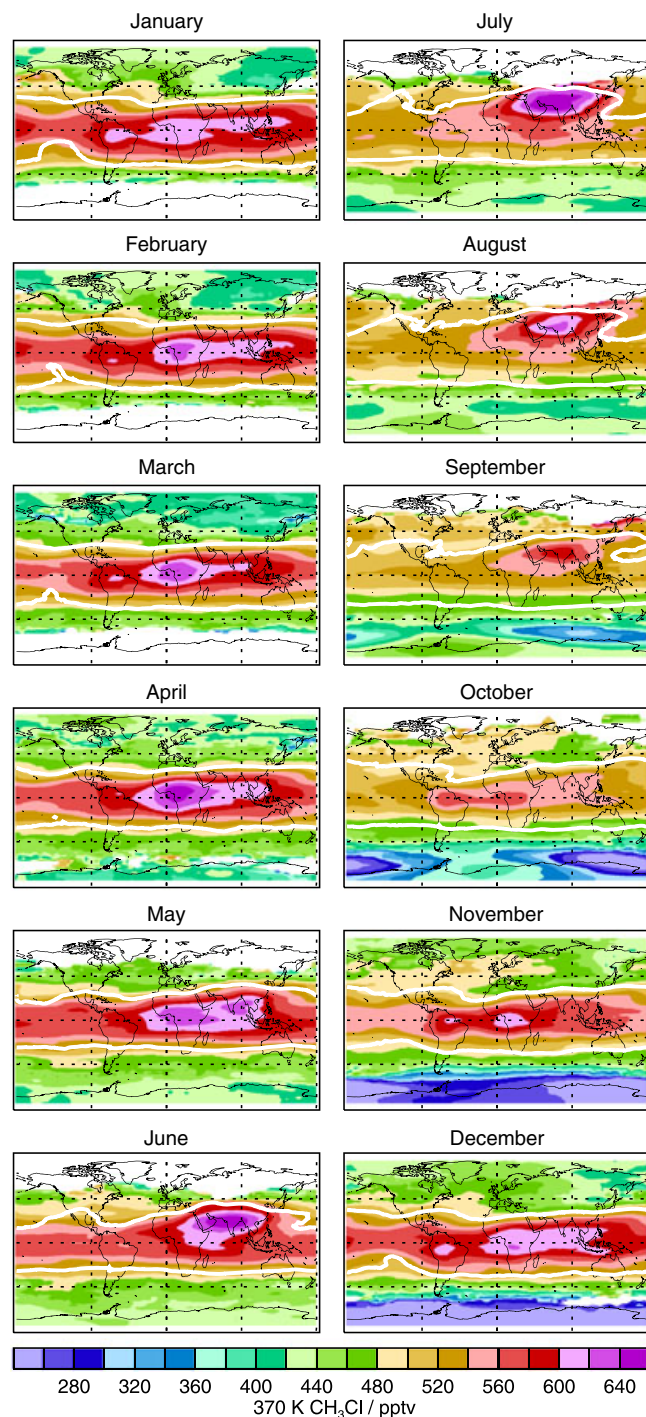
[30] Satellite measurements afford the opportunity for much more spatially and temporally extensive intercomparisons. The Atmospheric Chemistry Experiment Fourier Transform Spectrometer (ACE-FTS) on the Canadian Space Agency’s SCISAT-1 mission measures high spectral resolution (0.02 cm⁻¹) solar occultation spectra over the range 750–4400 cm⁻¹ (2.2 to 13.3 μm) [Bernath *et al.*, 2005]. Vertical profiles are retrieved for up to 15 sunrises and 15 sunsets per day, the latitudes of which vary over an annual cycle, allowing coverage from 85°S to 85°N with an emphasis on the polar regions during winter and spring. The vertical and horizontal resolution of the ACE-FTS measurements are 3–4 km and ~500 km, respectively [Boone *et al.*, 2005], slightly better than the corresponding values for the MLS CH₃Cl data. Velazco *et al.* [2011] performed noncoincident validation of version 2.2 ACE-FTS data by comparing against MkIV data from the September 2004 and 2005 balloon flights using a potential vorticity/potential temperature coordinate framework. They found that although differences between MkIV and ACE-FTS CH₃Cl were within ±30%, ACE-FTS consistently recorded values larger than those from MkIV below 450 K. In agreement with that finding and Figure 4, comparisons between coincident profiles over a 4 year period reveal a high bias in the version 3.0 (v3) ACE-FTS CH₃Cl data relative to MLS of 75–100 pptv (~20%) at 100–147 hPa (Figure 6; nearly identical results are obtained at pressures larger than 20 hPa for version 2.2 ACE-FTS data, not shown). ACE-FTS CH₃Cl is also substantially larger (differences of 90–120%) than that from MLS above 10 hPa; the increase in CH₃Cl indicated by the ACE-FTS profile in this region is not expected for a species with purely tropospheric sources. In contrast with the extremes of the profile, from 46 to 10 hPa the ACE-FTS CH₃Cl values are smaller than those from MLS by 10–40 ppt (5–85%). Thus, the overall shapes of the profiles from the two instruments are markedly dissimilar. The standard deviation about the mean differences is considerably smaller than the combined precisions of the two data sets (compare light blue solid and dashed lines) throughout the vertical domain.

[31] The MLS and ACE-FTS data sets are further intercompared in Figure 7. The data have been interpolated to the 370 K potential temperature surface and gridded into 5° bands of equivalent latitude (EqL), the latitude encircling the same area as a given contour of PV [Butchart and Remsberg, 1986], ensures that meteorologically similar air masses are averaged together. The gridding procedure involves taking weighted averages of all data points falling within prescribed envelopes in EqL and time (grid points at 1200 UT each day) of each grid location. A Gaussian weighting function with 2.5° latitude and 3.0 d time half widths is used; data within three half widths in both EqL and time are included in the average. In addition to being weighted by distance in space and time from each grid point, measurements are also weighted by their respective uncertainties, with a half width of

50 pptv. Although the error weighting allows inclusion of most measurement points, occasional poor-precision profiles falling far out in the wings of the Gaussian are given very little weight. Known “fliers” in the ACE-FTS data (https://database.scisat.ca/validation/data_issues_table.php) have been discarded. Figure 7a shows time series in two representative EqL bins: 30°N and 60°S. The sparsity of the ACE-FTS measurements renders comparisons at lower latitudes uninformative; even at 30°EqL it is difficult to draw definitive conclusions about their time evolution (despite the smoothing inherent in the gridding process), but the offset between the two data sets seen in Figure 6 appears to

vary only slightly with time at this latitude. In general, the bias is smaller at 60°EqL, and the seasonal variation in the two data sets is similar, although ACE-FTS fails to capture the pronounced minimum in CH₃Cl in late austral winter and spring (discussed further in section 4).

[32] Latitudinal slices through the data for representative days in all four seasons are shown in Figure 7b. Because the ACE-FTS sampling repeats from year to year, to make the comparison more robust, data from 2005 to 2009 have been averaged together for each of the dates shown; averages are computed only for latitude bins in which measurements from three or more years are available. Figure 7b shows that the offset between the data sets varies not only with latitude but also with time. The latitudinal gradients in the two data sets, however, are generally very similar. Finally, as discussed above, tracer-tracer correlation plots provide a valuable means of performing noncoincident validation. Figure 7c shows CH₃Cl/CO correlations over the entire 5 year interval, color coded by latitude. The more than 60,000 values in the gridded MLS field and almost 24,000 values in the gridded ACE-FTS field reveal strong correlations between the two species with similar linear fits in both data sets. On the basis of these comparisons, we conclude that MLS and ACE-FTS CH₃Cl measurements are in very good qualitative agreement in the UTLS.



4. Methyl Chloride Spatial and Temporal Variability in the UTLS

[33] To provide context for the MLS measurements of CH₃Cl in the UTLS, we first briefly review its spatial and seasonal patterns at lower levels. At the surface and into the free troposphere, the CH₃Cl distribution shows a distinct variation with latitude, with concentrations ~ 40 – 70 pptv higher in the equatorial regions than in the polar regions (compared to a surface mixing ratio of roughly 550 pptv on

Figure 8. Climatological monthly mean maps of MLS v3.3 CH₃Cl at 370 K averaged over 2005–2012. The along-track data are mapped onto a 2° latitude \times 5° longitude grid by taking a weighted average of all of the measurements on a given day within a specified distance of each grid point. A \cos^2 function is used for the weighting, with half-width values of 2° in latitude and 12° in longitude. Monthly means for individual years are computed by averaging the daily gridded data; in each year, any bin in which there are fewer than five measurements for a given month is filled with a bad data value. Yearly means are then averaged to produce the climatological values for each month. Note that 370 K corresponds approximately to 150 hPa or ~ 12 km in much of the extratropics, but is closer to 100–120 hPa or even lower pressures in the winter polar regions and the tropics; in the high temperatures of polar summer, however, the 370 K surface for the most part lies below the lowest level at which CH₃Cl is retrieved (147 hPa), and thus there are large blank areas in the maps in these regions. White lines show the monthly mean (2005–2012) $4.5 \times 10^{-6} \text{ K m}^2 \text{ kg}^{-1} \text{ s}^{-1}$ (4.5 PVU) GEOS-5 potential vorticity (PV) contour to identify the climatological dynamical tropopause.

average) [e.g., Yokouchi *et al.*, 2000; Yoshida *et al.*, 2004; World Meteorological Organization, 2011]. The latitudinal gradient at the surface is comparable in both hemispheres, consistent with the fact that its sources are primarily (>85%) concentrated in the tropics and subtropics [e.g., Khalil and Rasmussen, 1999; Yoshida *et al.*, 2004].

[34] Near-surface CH₃Cl also exhibits a pronounced annually repeating seasonal cycle [Cox *et al.*, 2003; Khalil and Rasmussen, 1999; Simmonds *et al.*, 2004; Yoshida *et al.*, 2004], with a late winter/early spring maximum and a late summer/early autumn minimum. The amplitude of the CH₃Cl seasonal cycle decreases with decreasing latitude, ranging from ~15% in the Northern Hemisphere polar regions to ~10% in the tropics, with the magnitude of the cycle only about half as large at corresponding latitudes in the Southern Hemisphere [Khalil and Rasmussen, 1999; Simmonds *et al.*, 2004; Yoshida *et al.*, 2004]. The marked seasonal variations in CH₃Cl arise through a variety of processes. Biogenic emissions represent the combined effects of fluctuations in parameters such as atmospheric temperature, precipitation, available light, etc. For example, CH₃Cl emissions from tropical plants in Africa are at a maximum from roughly November to January and at a minimum from roughly July to September, when very hot and dry conditions inhibit plant growth [Xiao *et al.*, 2010]. Oceanic CH₃Cl emissions tend to be largest during the spring, when wind speeds and sea surface temperatures are higher [Xiao *et al.*, 2010]. In contrast, the global CH₃Cl soil sink peaks during northern summer [Xiao *et al.*, 2010]. Biomass burning also has strong seasonal dependencies in various regions, as discussed further below. A major portion of the observed CH₃Cl seasonal variation is attributable to reaction with OH, which displays a similar interhemispheric difference in the amplitude of its seasonal cycle [e.g., Khalil and Rasmussen, 1999; Yokouchi *et al.*, 2000; Yoshida *et al.*, 2004].

[35] Spatial and seasonal variability in CH₃Cl similar to that at the surface is seen by MLS in the UTLS, at least in the tropics and subtropics. Figure 8, discussed in more detail in section 4.1, shows climatological (2005–2012) monthly mean maps of MLS CH₃Cl data interpolated to 370 K potential temperature. White overlays on the maps identify the approximate location of the climatological monthly mean dynamical (PV) tropopause. The exact definition of the dynamical tropopause remains somewhat subjective, and a wide range of PV values has been employed (e.g., see the discussion in Santee *et al.* [2011], and references therein). Scott *et al.* [2003] found that the region of weakest mixing indicative of the tropopause corresponds to PV values of ~4 PVU ($10^{-6} \text{ K m}^2 \text{ kg}^{-1} \text{ s}^{-1}$) in the Northern Hemisphere and ~5 PVU in the Southern Hemisphere during winter at 370 K. Accordingly, and as recommended by Haynes and Shuckburgh [2000] for the 370 K level, here we use the 4.5 PVU contour. As Figure 8 indicates, the 370 K surface, which corresponds approximately to the 147 hPa MLS retrieval pressure level (the lowest level at which CH₃Cl is retrieved), represents the upper portion of the lowermost stratosphere in the extratropics but is below the dynamical tropopause (as defined here) in the tropics. It should be noted that, as discussed in section 3, the retrievals at this level reflect non-negligible influence from the measurements at 100 hPa. However, much of the variability reported in the CH₃Cl data at 147 hPa is muted or absent in the retrievals

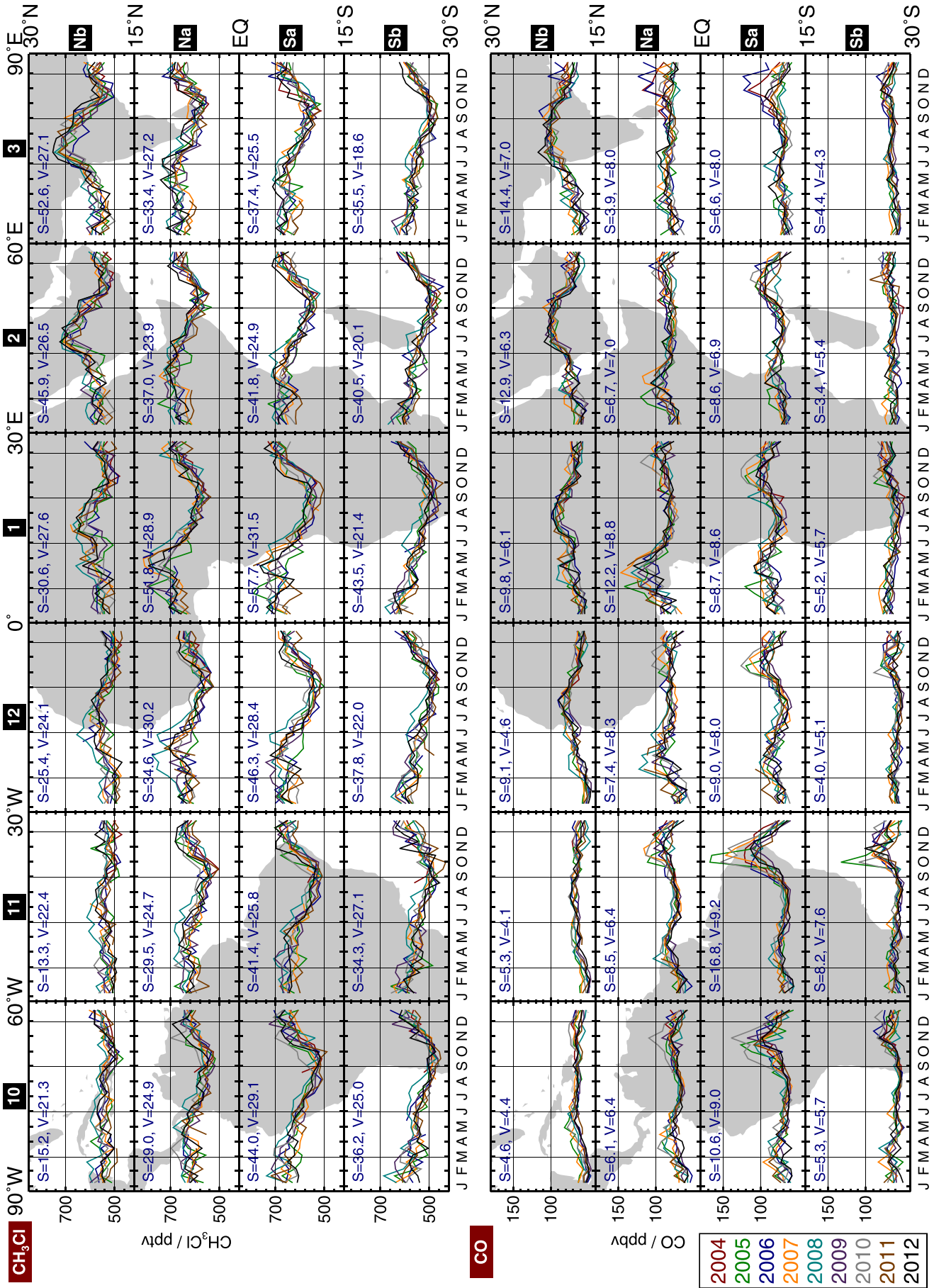
at 100 hPa, indicating that it most likely represents real atmospheric variations at the 147 hPa level.

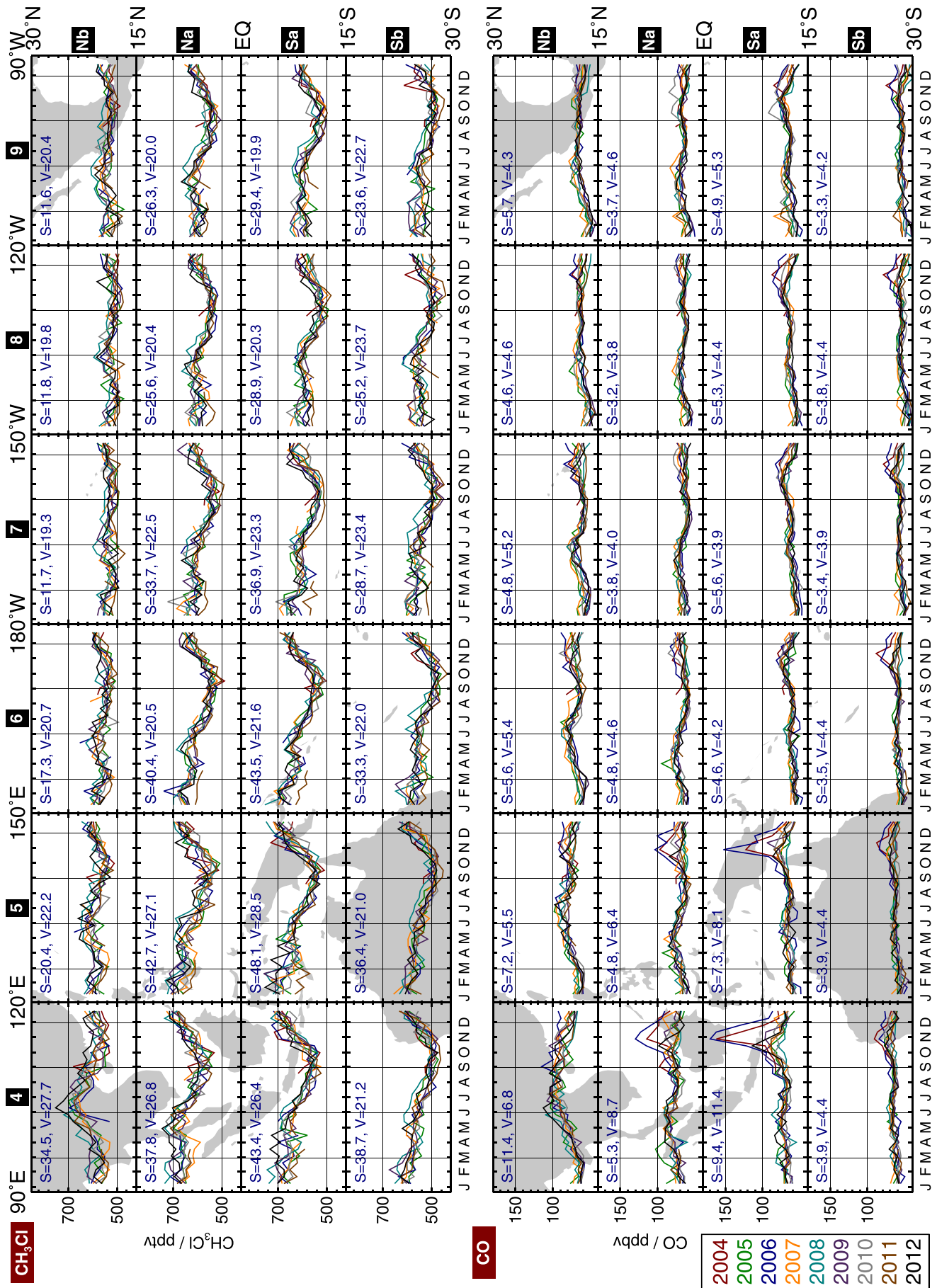
[36] The monthly maps are complemented by time series of regional (over 15° latitude × 30° longitude bins) biweekly averages of MLS CH₃Cl and CO measurements in the tropics and subtropics (30°S–30°N) at 147 hPa shown in Figure 9. Similar regional biweekly averages were presented for MLS O₃, CO, and cloud ice water content (IWC) at 215 hPa by Livesey *et al.* [2013a]. In order to characterize the observed variations in each region in Figure 9, an average annual cycle is computed as the multiyear mean in each of the 26 biweekly bins. An average seasonal cycle amplitude (S) is then defined as the standard deviation of this multiyear mean about its average. In addition, an average interannual variability (V) is defined by calculating, for each of the 26 fortnights, the standard deviation of the year-to-year variations about the multiyear average, then taking the root mean square average of the standard deviations in all 26 two week periods. (See Livesey *et al.* [2013a] for more details about the calculation of the S and V statistics.)

[37] As at the surface, the amplitude of the CH₃Cl seasonal cycle (S) at 147 hPa is ~10% or less throughout the tropics and subtropics (Figure 9). Distinct and annually repeating seasonal cycles are evident in almost all regions shown; only in parts of the northern subtropics (cells 5–11Nb) are the relatively small seasonal variations masked by larger year-to-year variations ($V > S$). Similar to the findings of Livesey *et al.* [2013a] (for the 215 hPa level), the MLS IWC data at 147 hPa (not shown) indicate that convection is generally strongest and has the largest seasonal cycle amplitudes over India (3Nb), southeast Asia (4Nb), the maritime continent (columns 3–6 in rows Na and Sa), northern and central South America (columns 10–11 in rows Na and Sa), and central Africa (1Na, 1Sa). Accordingly, these regions tend to have both the largest peak abundances of CH₃Cl and CO and the strongest and most repeatable seasonal cycles. Although these regions also exhibit the largest year-to-year variations, their seasonal cycle amplitudes tend to significantly exceed the degree of interannual variability ($S > V$).

4.1. Methyl Chloride as a Marker of Pollution

[38] Many factors contribute to the considerable variability in the tropics and subtropics seen in Figures 8 and 9. In addition to variations in biogenic processes as noted above, the geographical and seasonal patterns of biomass burning, convection, and large-scale ascent associated with the Brewer-Dobson circulation also play major roles. As is the case for other species, such as CO [e.g., Pickering *et al.*, 1996], lofting by deep convection (or other fast processes such as vertical transport driven by typhoons or warm conveyor belts ahead of cold fronts) can very rapidly inject CH₃Cl from biomass burning into the upper troposphere, where mixing ratios of more than 800 pptv have been observed in fresh coherent biomass burning plumes [Blake *et al.*, 1996; Rinsland *et al.*, 2007]. In fact, a strong linear correlation between CH₃Cl and CO has been observed in biomass burning plumes throughout the free troposphere [e.g., Blake *et al.*, 1996, 1997, 2001, 2003; Singh *et al.*, 2003; Rinsland *et al.*, 2007]. The high-resolution composite inventory of global annual CH₃Cl surface fluxes integrated over its individual sources is geographically inho-





mogeneous [Keene *et al.*, 1999], with peak emissions from biomass burning “hot spots” located in Southeast Asia, India, Indonesia, central Africa, and South America [Lobert *et al.*, 1999]. Although individual enhancements in fire-generated species observed by MLS in the UTLS can be attributed to specific burning events only in rare instances [e.g., Livesey *et al.*, 2004; Pumphrey *et al.*, 2011], Figure 8 shows that the biomass burning emissions hot spots are generally reflected in the larger CH₃Cl mixing ratios in the upper troposphere over those regions, depending on the time of year.

[39] Exact correspondence of the abundances of a relatively long-lived species such as CH₃Cl in the upper troposphere with its surface sources is not expected because the picture is complicated by the occurrence of horizontal transport either before or after the transport to those altitudes by convection and/or large-scale ascent. Jiang *et al.* [2007] analyzed Aura MLS measurements of CO (which has both industrial and biomass burning sources) and IWC (which serves as a proxy for deep convection) over Southeast Asia and the northern Pacific. They concluded that the distribution of CO in the upper troposphere (215–100 hPa) is controlled by the complex interplay between surface emissions, deep convection, and long-range horizontal transport. Other studies have investigated the CO distribution over South America, Africa, and Indonesia and reached the same conclusion [e.g., Duncan *et al.*, 2007; Barret *et al.*, 2008; Liu *et al.*, 2010]. A similar combination of factors governs the CH₃Cl spatial and temporal variations. Detailed examination of Figure 9 reveals, however, that although specific pollution events manifest frequently in both species, their different emissions sources lead to subtly different background seasonal variations. These patterns are explored in the following subsections. Several previously published modeling studies have elucidated the processes giving rise to the observed CO distribution; we discuss their results here to shed light on the behavior of CH₃Cl.

4.1.1. Climatological Seasonal Variations

[40] The African continent is typically the single largest source of biomass burning emissions, contributing on average about half of the global total, with relatively low year-to-year variation in fire activity [Duncan *et al.*, 2003; Schultz *et al.*, 2008; van der Werf *et al.*, 2010]. In Africa south of the equator, fires begin as early as May, reach their maximum extent in July and August, and subside by December [Duncan *et al.*, 2003; Liu *et al.*, 2010]. The MLS CH₃Cl measurements in Figures 8 and 9 exhibit a broad seasonal peak over southern Africa starting in October and generally persisting into June. A similar time lag between the peak in

fire emissions and the peak in CO in the upper troposphere in October/November has been attributed to subsidence over southern Africa inhibiting convection and trapping CO in the lower troposphere until the Intertropical Convergence Zone (ITCZ) migrates southward, bringing deep convection over this region in September and October [Liu *et al.*, 2010]. Apart from local fires, tagged model runs tracing emissions from individual sources indicate that fire pollution transported from South America also contributes to the CO maximum over southern Africa in October [Liu *et al.*, 2010]. Plumes from southern Africa and South America intermingle [e.g., Duncan *et al.*, 2007], and the connection between the two burning regions is clearly evident in the October and November climatological CH₃Cl maps (Figure 8; also seen in similar maps for CO, not shown). In addition, in some years, burning emissions from Indonesia transported westward may affect upper tropospheric CO abundances in September–November to an even greater extent than those from southern Africa itself [Liu *et al.*, 2010]. Unlike CH₃Cl, CO displays a double-peak structure, with lower values from December to March and then a weak secondary maximum over southern Africa in April that simulations show originates from burning in northern Africa, again with occasional contributions from fires in Indonesia [Liu *et al.*, 2010]. In contrast, CH₃Cl abundances remain high over this region for much of the year, dropping precipitously in austral winter. Since biomass burning and dynamical processes affect the CH₃Cl distribution in the UTLS in the same manner as for CO, it is noteworthy that the CH₃Cl and CO seasonal cycles depart noticeably in southern and central Africa. This difference in behavior between the two species most likely arises because CH₃Cl is more strongly influenced by biogenic processes than is CO. Emissions from tropical plants in Africa are at a maximum in December, whereas they are at a minimum from around July through September, when consumption by microbial processes in soils is at a maximum [Xiao *et al.*, 2010].

[41] In Africa north of the equator, fires occur mainly from November through March, with widespread burning ending by April [Duncan *et al.*, 2003, 2007]. With little deep convection to carry it aloft in the first few months of the fire season, much of the pollution from local fires initially disperses in the boundary layer. On the basis of modeling results for CO [Duncan *et al.*, 2007; Liu *et al.*, 2010], we expect that the perturbation in CH₃Cl in the upper troposphere and near the tropopause from northern African burning emissions is at its maximum from February to May, as vigorous seasonal convection occurs with the advance of the ITCZ northward over central Africa. A weak secondary

Figure 9. (top) MLS v3.3 CH₃Cl and (bottom) CO observations at 147 hPa from 90°W to 90°E (first page) and from 90°E to 90°W (second page) over the tropics (30°N–30°S). Each cell displays time series of biweekly averages of MLS data in that geographical region covering the period from August 2004 through December 2012. Month labels are provided at the bottom of each set of panels, with thin vertical lines drawn at the beginning of March, June, September, and December to guide the eye. Different years are represented by different colored lines as indicated in the legend. Numbers and letters in black boxes along the top and right edges of the panels provide unique identifiers for each individual cell. Metrics characterizing the amplitude of the seasonal cycle (S) and the interannual variability about that seasonal cycle (V) are given in each cell, in the same units as the y axes. See text and Livesey *et al.* [2013a] for more details on the calculation of the regional biweekly averages, as well as S and V . Typically, 200–300 profiles contribute to each biweekly average in each region, leading to precisions of ~ 10 pptv for the CH₃Cl averages and ~ 1 ppbv for CO.

CH₃Cl maximum occurs in the upper troposphere over the northern part of central Africa in October–December; a similar feature in CO has been attributed to convective uplift of air rich in pollutants from burning in southern Africa, South America, and Indonesia [Liu *et al.*, 2010]. In addition, Barret *et al.* [2008] argue that the distribution of CO at and above (i.e., at pressures less than) 150 hPa over northern Africa (25°–35°N) in summer is mainly driven by the influx of polluted air masses originating in Asia that have been lofted to the upper troposphere, confined within the Asian summer monsoon anticyclone, and then transported westward by the tropical easterly jet. Long-range transport of Asian pollution may similarly affect the CH₃Cl over northern Africa in summer.

[42] South America typically contributes as much as a quarter of global fire emissions, although it exhibits substantial interannual variability in biomass burning [Duncan *et al.*, 2003; Schultz *et al.*, 2008; van der Werf *et al.*, 2010]. Burning generally begins in July, about 2 months later than in southern Africa, peaks in August and September, and dies down by November as the ITCZ shifts southward [Duncan *et al.*, 2003, 2007; Liu *et al.*, 2010]. The southward progression of the wet season over the continent not only extinguishes the fires but also leads to rapid increases in vertical air mass flux, through both convection and slower large-scale advection [Liu *et al.*, 2010]. The modeling study by Duncan *et al.* [2007] showed that tropical easterlies transport much of the surface pollution from southern Africa and South America to the Pacific Ocean. A broad area of convection extending from western Africa across South America to the central Pacific lofts the biomass burning emissions to the upper troposphere, where they are advected by the southern subtropical jet, causing significant perturbations in trace gas distributions over much of the tropics at the tropopause and into the lower stratosphere from September through December. Figure 9, however, shows that MLS CH₃Cl at this altitude displays a temporally broad peak, with mixing ratios remaining elevated over South America continuously from October through May. In contrast, CO reaches its seasonal maximum in the upper troposphere over South America in October and November. Although a much smaller secondary maximum in CO does occur over South America in February to May (caused in part by biomass burning in northern Africa [Liu *et al.*, 2010]), the temporal evolution of CO is quite different from that of CH₃Cl. Again, the more persistent enhancement in CH₃Cl over South America most likely arises from biogenic emissions.

[43] Finally, although the burning season in Southeast Asia runs from January to May, it peaks sharply in March, when approximately 50% of the biomass burning in the region takes place [Duncan *et al.*, 2003, 2007]. Model simulations have shown that prevailing winds advect the surface pollution to the Indian and Pacific Oceans, where it is lofted to the upper troposphere by convection over the Bay of Bengal and the South China Sea [Duncan *et al.*, 2007]. The northern subtropical jet then rapidly transports the pollution around the globe, leading to perturbations in the CH₃Cl distribution at the tropopause over most of the Northern Hemisphere tropics and subtropics in boreal spring, as has been reported for CO [Duncan *et al.*, 2007].

[44] At 147 hPa, strong enhancements in both CH₃Cl and CO occur over the entire southern Asian region dur-

ing summer of every year (see climatological maps and also cells 3Nb and 4Nb of Figure 9). Consistent with that picture, Livesey *et al.* [2013a] found that the most persistent and repeatable strong enhancements in CO at 215 hPa occurred over the Asian monsoon region from June to September. Pollution transported upward by deep convection over the monsoon region and the Tibetan Plateau becomes trapped within the monsoon anticyclone in the UTLS [e.g., Li *et al.*, 2005; Fu *et al.*, 2006; Park *et al.*, 2007, 2009; Randel *et al.*, 2010]. Most of the pollution lofted into the upper troposphere over India and China during the summer monsoon season is anthropogenic in origin (i.e., from industrial emissions, domestic biofuel consumption, etc.) rather than arising from biomass burning, which is largely extinguished by the heavy precipitation at that time [e.g., Jiang *et al.*, 2007]. A few previous studies have linked CH₃Cl enhancements in the UTLS to monsoon-related convective transport of boundary layer pollution. ACE-FTS measurements have indicated a persistent maximum in CH₃Cl inside the chemically isolated monsoon anticyclone over the ~14–18 km altitude range [Park *et al.*, 2008]. Enhanced mixing ratios of CH₃Cl and other surface pollutants measured in the lowermost stratosphere over the eastern Mediterranean in August have been linked to long-range transport of outflow from the Asian summer monsoon [Scheeren *et al.*, 2003].

4.1.2. Interannual Variability

[45] Although many features recur every year, strong enhancements in CH₃Cl and CO present in some years are much weaker or even absent in others. Of course, biogenic processes vary from year to year; in particular, heat and drought reduce the growth of plants [e.g., Ciais *et al.*, 2005] and thus their emissions. Interannual variability in the frequency and strength of convective updrafts and, more importantly, shifts in the locations of deep convection in relation to major sources influence the composition of the UTLS [Duncan *et al.*, 2007]. Year-to-year changes in the ascent rate associated with the Brewer-Dobson circulation may also play a minor role [Duncan *et al.*, 2007]. But the substantial interannual variability in biomass burning [Duncan *et al.*, 2003; Schultz *et al.*, 2008; van der Werf *et al.*, 2010] is most likely the largest contributor to the observed variation in trace gas distributions near the tropopause. Large-scale biomass burning episodes have been shown to increase CH₃Cl emissions and strongly affect its interannual variability on a global scale [Simmonds *et al.*, 2004, 2005; Trudinger *et al.*, 2004]. In addition to Figure 9, the anomaly maps of Figure 10 illustrate the interannual variability in upper tropospheric CH₃Cl abundances by showing departures from the climatological mean for selected months. Despite the imposition of quality control measures, some of the anomalies in Figure 10, especially those that are smaller in magnitude or more localized in space and time, may arise from data artifacts, but most of them likely reflect real atmospheric signatures. Here we discuss a few of the individual features that particularly stand out in Figure 10. We note that for brevity, similar anomaly maps for CO are not shown, but with few exceptions (noted below) the major aspects of Figure 10 highlighted here are evident in both the CH₃Cl and the CO distributions.

[46] An extreme enhancement in upper tropospheric CH₃Cl is seen over central Africa in February 2005 (also

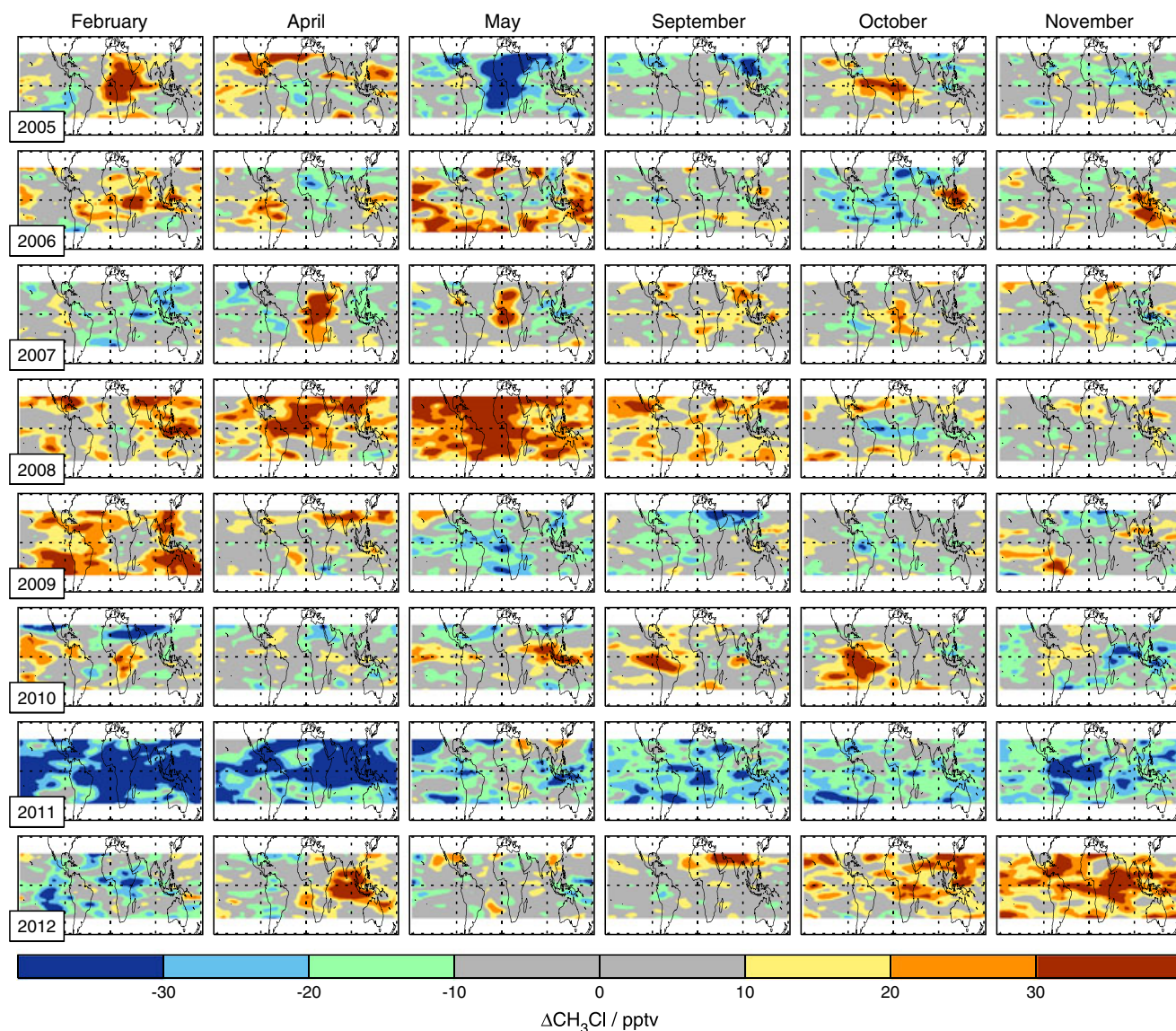


Figure 10. Absolute differences (pptv) between monthly mean MLS CH₃Cl and the climatological monthly values in Figure 8 at 370 K for selected months and all years from 2005 to 2012. For clarity, only tropical (30°N–30°S) values are shown.

present in CO; see cells 1Na and 1Sa of Figure 9). Biomass burning produces a robust signature at this time/place in the climatological maps (Figure 8), but the magnitude of the 2005 increase far exceeds that in either species in any other February during the Aura era. Although similar enhancements occur at 100 hPa (not shown), they are not present in the CO at 215 hPa [Livesey *et al.*, 2013a]. The MLS IWC data (not shown) suggest that the exceptionally large upper tropospheric abundances of CO and CH₃Cl may be related to anomalously strong convection at this time. Liu *et al.* [2010] reported that the CO maximum at 147 hPa in February was much larger in 2005 than in 2006 in both MLS data (version 2.2) and results from the GEOS-Chem chemistry transport model driven by assimilated meteorological fields. They attributed the uncommonly large enhancement in 2005 to a combination of higher fire emissions in January–February and enhanced vertical mixing (from convection

and/or advection) over the Gulf of Guinea in February of that year.

[47] Exceptional enhancements over a wide swath of central Africa are also seen in April and May 2007 (Figures 9 and 10). Although CO emissions as reflected in the Global Fire Emissions Database [(version 3, GFED3), van der Werf *et al.*, 2010] are moderately high in northern Africa in late 2006 and early 2007 (not shown), they do not appear to be large enough to account for the magnitude of the anomalies present in MLS measurements of CO and CH₃Cl in the upper troposphere. However, GFED3 CO emissions are atypically large in southern Africa in February 2007, at a time when MLS IWC data (not shown) suggest that convection was relatively strong in that region.

[48] As discussed above, a broad maximum in CH₃Cl persists over South America (Figure 9, columns 10–11, rows Na, Sa, and Sb) from roughly October through May every

year, reflecting not only biogenic emissions, but also intense biomass burning in the preceding months in conjunction with the onset of convection. However, over much of the region, the increases in 2005 and 2010 are larger and, particularly in 2010, commence earlier (September) than those in other years observed by MLS (see also Figure 10). Similar behavior is seen in CO, which also exhibits higher values in 2007 and, to a lesser extent, 2004 (Figure 9, 11Sa). The enhancements over South America are especially strongly connected to similar increases over central Africa in October and November of those years. High-fire years in South America are frequently associated with low levels of precipitation, which is suppressed when sea surface temperatures in the tropical eastern Pacific and North Atlantic are anomalously high [e.g., *Chen et al.*, 2011, and references therein]. The years 2004, 2005, 2007, and 2010 were all characterized by severe fire seasons in the Amazon [*Chen et al.*, 2011], resulting in extremely high GFED3 CO emissions. Exactly why the intense burning in 2007, which resulted in the highest fire emissions in this region of any year in the GFED3 record except for 2010 (not shown), apparently produced strong enhancements in CO but not CH₃Cl remains to be investigated. In contrast to the high-fire years, lower burning emissions related to the El Niño caused CO (and presumably CH₃Cl as well) to be depressed over South America in October 2006 relative to that in October 2005 (a neutral El Niño year) [e.g., *Logan et al.*, 2008]. Consistent with the smaller UTLS abundances in October in Figures 9 and 10, 2008 and 2009 were also low-fire years in this region [*Chen et al.*, 2011; *van der Werf et al.*, 2010]; a substantial enhancement in both species in November 2009 most likely arises from extraordinarily strong convection (i.e., high IWC, not shown) in this region during the preceding month.

[49] Another notable feature is the enhancement in upper tropospheric CH₃Cl in the vicinity of Indonesia in October and November 2006 (Figure 10 and cells 3–5Na/Sa of Figure 9). Even more dramatic enhancements appear in the CO data at 147 hPa at this time and location, as well as at 215 hPa [*Livesey et al.*, 2013a]. These signatures reflect increased emissions related to the moderate El Niño of 2006. A strong correlation with the El Niño–Southern Oscillation signal exists for fires in Indonesia and Malaysia [*Duncan et al.*, 2003, 2007; *Schultz et al.*, 2008]. El Niño perturbs convective patterns and the large-scale circulation in the tropical Pacific, with consequent impacts on the composition of the upper troposphere. In particular, the dynamical changes, severe drought, and ensuing large-scale forest fires in Indonesia induced by the 2006 El Niño have been conclusively linked to substantial anomalies in tropospheric O₃, CO, and H₂O in October to December of that year [e.g., *Logan et al.*, 2008; *Chandra et al.*, 2009]. The fact that the positive phase of the Indian Ocean Dipole coincided with the 2006 El Niño event exacerbated the severity of the drought and hence the burning-related emissions [*Nassar et al.*, 2009]. The inversion analysis of *Xiao et al.* [2010] demonstrated that the heat and drought associated with El Niño events influence multiple processes, increasing CH₃Cl emissions from coastal salt marshes as well as from biomass burning, while decreasing microbial CH₃Cl consumption in soils (leading to larger atmospheric abundances) as well as emissions from tropical plants. The net effect is a transient increase in upper tropospheric CH₃Cl over

Indonesia in late 2006 (Figures 9 and 10), which mirrors those reported previously for CO and O₃. A relatively weak El Niño in the latter half of 2004 led to smaller and less extensive perturbations in tropospheric composition [*Logan et al.*, 2008; *Chandra et al.*, 2007, 2009], but its effects are also evident in the CH₃Cl and CO mixing ratios over Indonesia (Figure 9). Slight increases in CH₃Cl and CO in October and November 2009 (Figure 10 and 4–5Na/Sa of Figure 9) are also likely associated with an El Niño in that year. Toward the east in the central Pacific (Figure 9, 7Na/Sa), high IWC in early 2005, 2007, and 2010 (shown at 215 hPa by *Livesey et al.* [2013a]) is indicative of El Niño-related shifts in convection; the enhanced convective activity is manifested in higher values of CH₃Cl in and downstream of this region, at least in the latter 2 years.

[50] Methyl chloride abundances are exceedingly large in the UTLS over Indonesia and Malaysia in March and April 2012 (Figures 9 and 10). Although biomass burning is not uncommon in that season [*Duncan et al.*, 2003], the emissions in spring 2012 appear to have been particularly high. The severe pollution was in all likelihood connected to land-clearing fires set by palm oil companies in the peat swamp forests in Aceh province [*Cramb and Curry*, 2012; *Reid et al.*, 2012; *Widayati et al.*, 2012]. Raging forest fires in Indonesia in the fall of 2012 also led to conspicuously high CH₃Cl in October and November despite the absence of El Niño conditions at that time (e.g., http://www.cpc.ncep.noaa.gov/products/analysis_monitoring/enso_advisory).

[51] Episodes of substantially suppressed CH₃Cl mixing ratios are also evident in Figures 9 and 10. For example, the low values over much of the African continent in May 2005 are particularly noteworthy; CO abundances there are also slightly smaller than usual at that time. Fire emissions, which as discussed above had been extremely high in Africa in January and February 2005, were lower than those in most other recent years in March and April, according to GFED3. Moreover, the IWC values over central Africa were the lowest in the MLS data record for that region in April and May 2005. The combination of little fire pollution and weak convective activity apparently resulted in a marked reduction in upper tropospheric CO and CH₃Cl abundances.

[52] One puzzling aspect of these figures is that in many regions, the CH₃Cl mixing ratios are higher throughout much of 2008 than they are in any of the other years. The unusual behavior in 2008 is most readily perceptible in the February–September monthly means of Figure 10, but it is conspicuous in most of the cells in Figure 9 as well. Although MLS observed anomalously high IWC indicative of strong convective activity over central Africa in March and May 2008 (not shown), for the most part, the elevated CH₃Cl abundances in 2008 are not clearly associated with deep convection, nor do the corresponding MLS CO values mirror the CH₃Cl behavior in most cases. In addition, fire emissions in 2008 were below average in almost all regions of the globe, with the exception of boreal Asia [*van der Werf et al.*, 2010]. Proper attribution of these (and other) CH₃Cl enhancements will require detailed modeling studies beyond the scope of the present analysis.

[53] Finally, with few exceptions (e.g., parts of Africa and Asia in May), in 2011 CH₃Cl mixing ratios are lower than the climatological mean at almost all times and locations,

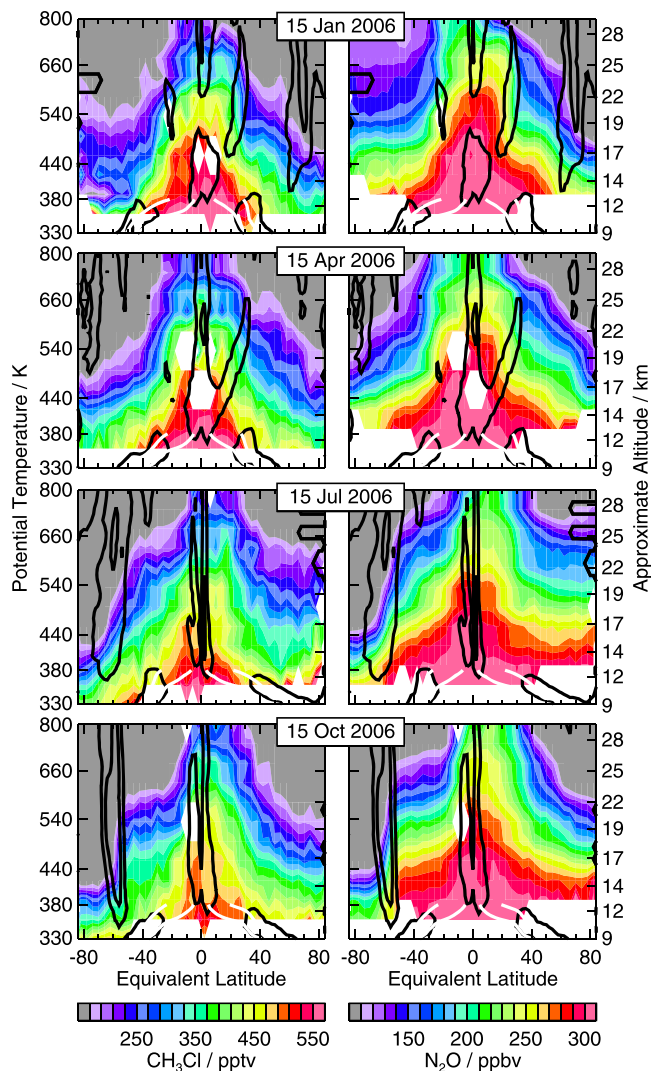


Figure 11. Equivalent latitude/potential temperature (EqL/ θ) cross sections of v3.3 MLS (left) CH₃Cl and (right) N₂O, for a representative day in each season for a typical year (2006). The vertical domain of the panels spans the range from roughly 130–220 hPa (330 K) to 5–10 hPa (800 K), depending on the temperature; corresponding approximate altitudes (for the extratropics) are given on the right-hand axis. Black contours show GEOS-5 normalized PV gradients of 1.5 and 4.5; the PV gradients are normalized by the hemispheric mean at each level, so values greater than 1 indicate stronger-than-average gradients, representing the upper tropospheric subtropical jet and stratospheric winter polar vortices. White contours show 1.5 and 4.5 PVU values to delineate the tropopause; note that these contours terminate at 380 K, the isentropes that typically corresponds to the tropical tropopause. The sharp cutoff in the CH₃Cl panels arises because MLS CH₃Cl is not retrieved at pressures larger than 147 hPa, and thus, these data are not available at the lowest potential temperatures except in the coldest regions at middle and high latitudes during winter. The cutoff occurs at higher levels in the N₂O panels because MLS N₂O data are not recommended below (i.e., at pressures larger than) 100 hPa.

often considerably so (Figures 9 and 10). Carbon monoxide abundances are also smaller than average. MLS IWC measurements do not indicate that convective activity was abnormally weak (not shown); if anything, convection was relatively vigorous over many areas in the first half of the year. Although GFED3 data suggest that fire seasons were not particularly quiescent in most regions in 2011, CO emissions were unusually low in South America that year. Below-average biomass burning activity in South America may have had near-global impact on upper tropospheric trace gas abundances in 2011.

4.2. Methyl Chloride as a Tracer of Large-Scale Transport

[54] The previous section highlighted the utility of CH₃Cl for tracking the lofting of pollution by deep convection. With its relatively long lifetime and tight correlation with N₂O [e.g., Avallone and Prather, 1997; Schauffler *et al.*, 2003, see also Figure 5], CH₃Cl should also be of use as a tracer of dynamical and transport processes in the upper troposphere and stratosphere.

4.2.1. Descent and Mixing

[55] Figure 11 shows equivalent latitude/potential temperature (EqL/ θ) cross sections of MLS CH₃Cl and N₂O for a representative day in each season for a typical year (2006). The cross sections are computed using the procedure described by Santee *et al.* [2011], and references therein. Although the v3.3 MLS N₂O data have better precision than the CH₃Cl data, they have comparable vertical resolution in the UTLS. The general morphology and temporal evolution of the two species show excellent correspondence, with many transient features seen in both sets of “snapshots”. In particular, the progressively steeper downward slope in the middle- and high-latitude contours from summer to winter in both species is indicative of strong diabatic descent inside the stratospheric polar vortices in both hemispheres. In fact, qualitatively, the best agreement between the two species is obtained where/when their morphology is determined primarily by descent. Since CH₃Cl and N₂O have different vertical and horizontal gradients, mixing processes may give rise to differences in their distributions. Overall, because MLS N₂O data are not recommended for scientific studies at pressures greater than 100 hPa [Livesey *et al.*, 2013b], we conclude that, despite its poorer precision, MLS CH₃Cl is a more useful tracer of air motions in the UTLS than is MLS N₂O.

[56] Next we investigate the EqL-mean evolution of CH₃Cl over the Aura mission (through 2012) at several potential temperature surfaces in the upper troposphere and stratosphere. As discussed in detail by Santee *et al.* [2011], it is instructive to compare the temporal variations in trace gas distributions observed by MLS with the seasonal and interannual variability in the strength of transport barriers diagnosed using meteorological analyses. Figure 12 shows time series of effective diffusivity, κ_{eff} , calculated on a 4° EqL grid from analyzed PV. Large values of κ_{eff} identify regions of strong mixing (weak transport barriers); small values identify regions of weak mixing (strong transport barriers). Corresponding time series of MLS CH₃Cl are given in Figure 13 (produced as described by Santee *et al.* [2011]). To facilitate interpretation, two contours of κ_{eff} (thin black lines) highlighting the regions of strongest mixing are

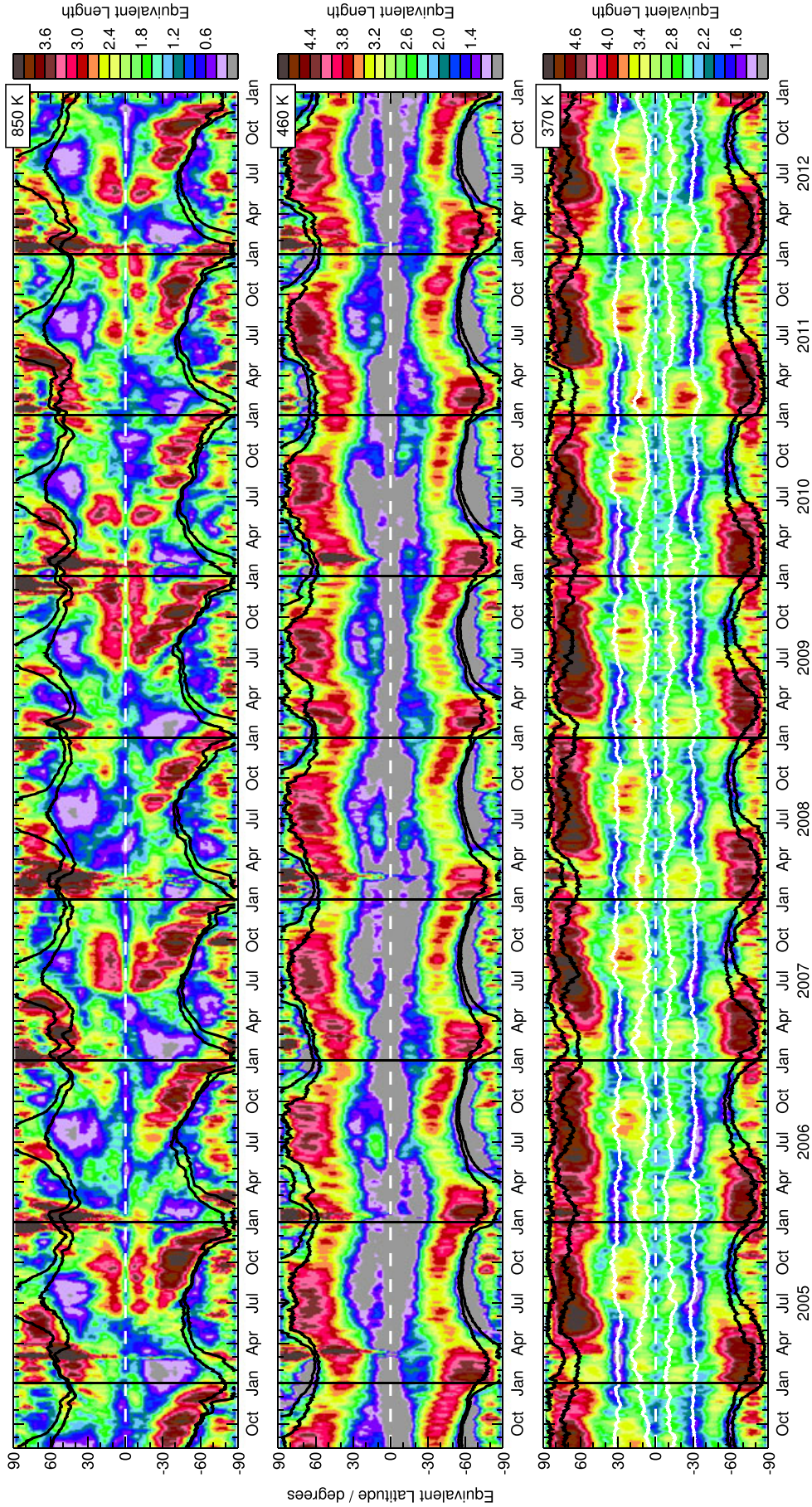


Figure 12. EqL-mean time series at 850, 460, and 370 K of effective diffusivity (κ_{eff} , expressed as log-normalized equivalent length) calculated from GEOS-5 Modern-Era Retrospective Analysis for Research and Applications (MERRA) PV. Black contours show the GEOS-5 1.2 and $1.4 \times 10^{-4} \text{ s}^{-1}$ values of scaled PV (sPV, calculated using the method of *Manney et al.* [1994]) to mark the polar vortex boundary; two contours are shown to indicate the steepness of the PV gradient and thus the strength of the transport barrier at the vortex edge. White contours at 370 K show the 1.5 and 4.5 PVU values to bound the tropopause. The vertical black solid lines denote year boundaries, and the horizontal white dashed lines denote the equator.

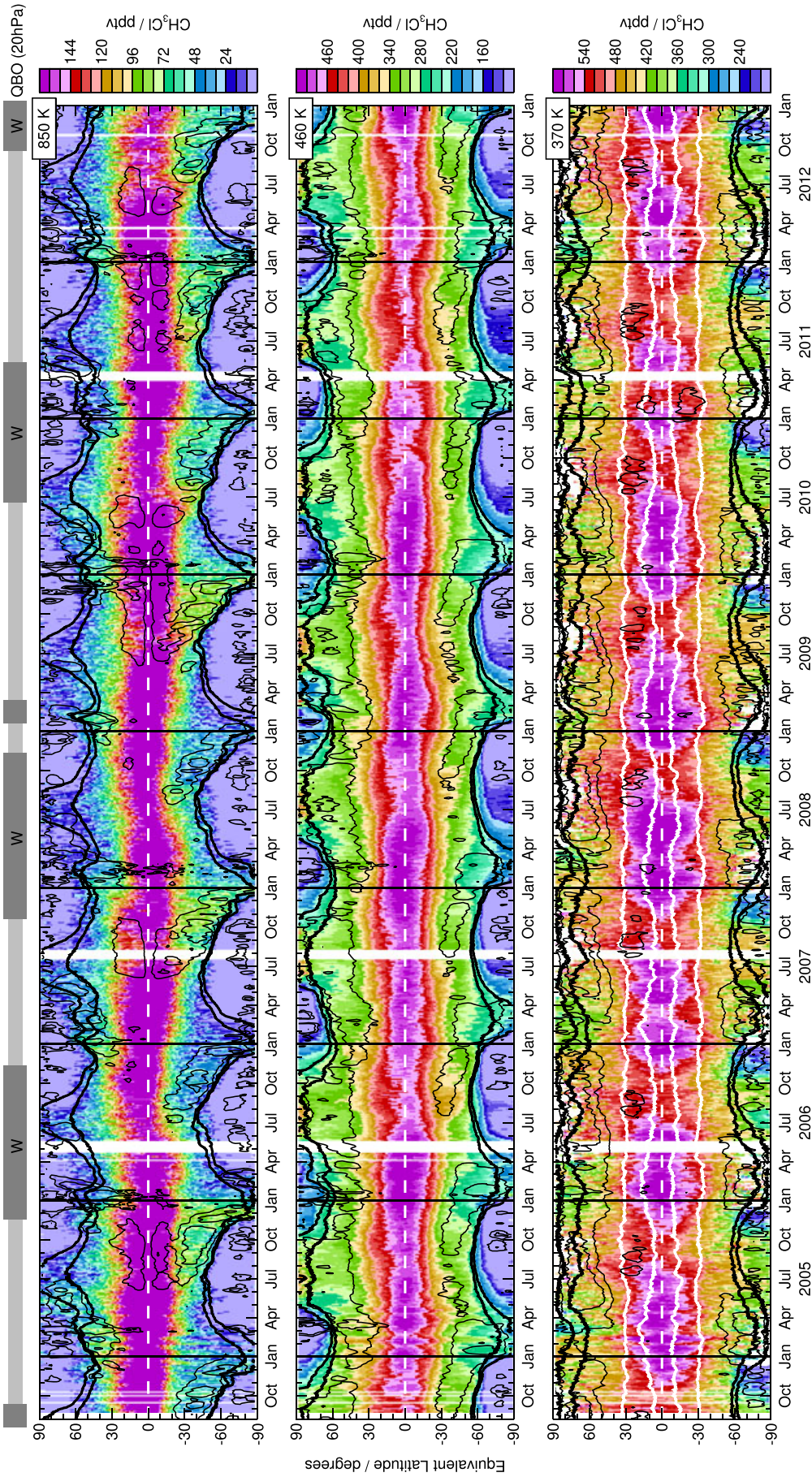


Figure 13. As in Figure 12, but for MLS CH₃Cl. Blank spaces represent missing MLS data. Note that the gridding in time performed to construct these plots fills in the highest-EqL bins to a greater extent than in the monthly mean maps of Figure 8. Also overlaid (thin black lines) are two contours of κ_{eff} (2.6 and 3.6 at 850 K, 3.4 and 4.4 at 460 K, and 3.6 and 4.6 at 370 K) to highlight regions of particularly strong mixing. Dark grey bars above the top panel identify the intervals during which the quasi-biennial oscillation (QBO) is in the westerly phase, as defined by Singapore (1°N/104°E) winds [e.g., *Naujokat*, 1986, <http://www.geo.fu-berlin.de/met/ag/strat/produkte/qbo/singapore.dat>] at 20 hPa (chosen because it is the level at which the magnitude of the Southern Hemisphere QBO response is maximum [*Baldwin and Dunkerton*, 1998]).

overlaid on the CH₃Cl time series plots, along with two contours of scaled PV (sPV, thick black lines) to mark the approximate boundary of the winter polar vortex and, at 370 K, two contours of PV (white lines) to bound the dynamical tropopause.

[57] Looking first at the polar regions, steep sPV gradients and low κ_{eff} values reflect the substantial barrier to meridional exchange provided by the vortex edge in mid-winter (Figure 12). Mixing is typically inhibited to a far greater extent in the Antarctic than in the Arctic at all levels. A distinct minimum appears in CH₃Cl in these regions in winter and spring, with the exact timing depending on the level (Figure 13). As mentioned in connection with Figure 11, this seasonal minimum in each hemisphere results from confined diabatic descent inside the winter polar vortices bringing down air poor in CH₃Cl from above; weaker descent at lower levels leads to a slight lag in reaching the minimum at successively lower isentropes. Interannual variability is considerable, especially at the lower two levels in the Arctic, with the signature of descent in the CH₃Cl field more evident in relatively cold and quiescent years and less clear in the dynamically disturbed winters of 2005/2006, 2008/2009, and 2009/2010, which all saw strong, prolonged major stratospheric sudden warmings [Manney *et al.*, 2009a, 2009b; Labitzke and Kunze, 2009; Lee *et al.*, 2011; Kuttippurath and Nikulin, 2012], with concomitantly strong mixing during those episodes. The abrupt increase in κ_{eff} and divergence of the sPV contours at the end of winter in both hemispheres signal the collapse of the transport barrier as the polar vortex breaks down (Figure 12). Santée *et al.* [2011] used MLS measurements of the stratospheric tracers O₃, HNO₃, and HCl to describe the export of polar-processed, ozone-depleted air from the eroding vortex at 370 K, and its effects on extravortex trace gas concentrations. The outflow from the decaying vortex can likewise be seen in the spread of low CH₃Cl abundances toward lower latitudes. This characteristic pattern of efflux of CH₃Cl-poor air from the vortex is particularly clear at 460 K in the abrupt changes in the extravortex contours starting in March or April in the Northern Hemisphere and in November or December in the Southern Hemisphere in most years. Similar signatures of mixing are also evident at 370 K, especially in the Southern Hemisphere.

[58] Turning to the tropics, in the UTLS CH₃Cl is characterized by marked maxima from about October or November through June or July every year. As discussed in connection with the climatological monthly mean maps of Figure 8, these recurring features reflect in part the seasonal cycles in the strengths of the CH₃Cl surface sources and convection. However, quasi-horizontal cross-tropopause transport and mixing also play a major role in governing the CH₃Cl distribution, especially at 370 K. The periodic minima at the equator roughly coincide with the seasonal weakening of the subtropical jet/tropopause transport barrier (see Figure 12 and the κ_{eff} overlays in Figure 13). Santée *et al.* [2011] showed that large abundances of O₃, HNO₃ and HCl, more typical of the stratosphere, regularly intrude into the tropical tropopause region at 370 K in a pattern indicative of stratosphere-to-troposphere transport events associated with the summer monsoon circulations. Unlike for the stratospheric tracers shown by Santée *et al.* [2011], such cross-tropopause exchange leads to reductions in the equa-

torial mixing ratios of a tropospheric tracer like CH₃Cl, as seen in Figure 13. Similarly, Santée *et al.* [2011] reported slightly smaller values of 370 K O₃, HNO₃, and HCl in the region just poleward of the tropopause in both hemispheres in their respective summers and attributed those variations to monsoon-related quasi-isentropic transport of tropical tropospheric air into the lowermost stratosphere. This interpretation is confirmed by the evolution of CH₃Cl in Figure 13, which shows apparent summertime incursions of tropical air into the extratropics. Such tropopause-level in-mixing from the tropics, which is seen in both hemispheres but is particularly striking in the north, leads to larger extratropical abundances of CH₃Cl at this time.

4.2.2. QBO and Tropical Tape Recorder Effects

[59] Another source of tropical trace gas variability is the quasi-biennial oscillation (QBO), characterized by downward-propagating easterly and westerly wind regimes that alternate approximately every 28 months on average [e.g., Baldwin *et al.*, 2001]. The QBO also exerts significant influence on the distributions of long-lived trace gases in the extratropics. A QBO signal has previously been identified in the stratosphere in several trace gases, with the sign and magnitude of the anomaly depending on the species' vertical mixing ratio gradient and the phase of the QBO [e.g., Chipperfield and Gray, 1992; Schoeberl *et al.*, 2008; Baldwin *et al.*, 2001].

[60] In the westerly QBO phase, planetary waves can propagate from the winter extratropics into the tropics and even penetrate into the summer hemisphere, where they break and cause increased mixing, whereas easterly QBO winds confine planetary wave activity to the winter extratropics, leading to greater mixing there as the waves break [e.g., Shuckburgh *et al.*, 2001; Garny *et al.*, 2007]. Such a QBO signal is evident in the distinctly enhanced transport of CH₃Cl from the tropics to high southern latitudes at 850 K in easterly QBO years (Figure 13). One apparent exception to the pattern of enhanced mixing in alternating southern winters is 2010, when the QBO phase shifted from easterly to westerly in June. An unusually strong midwinter minor stratospheric sudden warming developed in early July 2010, and the Antarctic stratosphere remained perturbed for more than a month, with associated anomalous poleward transport of lower-latitude air in the middle stratosphere and a consequent reduction in the severity of the ozone hole that year [de Laat and van Weele, 2011; Klekociuk *et al.*, 2011]. The larger CH₃Cl abundances flowing poleward at 850 K through the end of the year in 2010 compared to those in other Antarctic winters during westerly QBO regimes suggest that strong influx from the tropics to higher latitudes may have persisted well beyond the time frame of the warming.

[61] Long-lived trace gases whose mixing ratios at the tropical tropopause vary seasonally display a "tape recorder" signature as the variations are carried coherently upward into the stratosphere in the ascending branch of the large-scale Brewer-Dobson circulation [e.g., Schoeberl *et al.*, 2006, 2008]. The tape recorder was first identified as the imprint of vertically propagating seasonal oscillations in water vapor induced by variations in tropical tropopause temperatures [Mote *et al.*, 1996]. A tape recorder-like signal was subsequently identified in Aura MLS CO measurements, attributable in part to the seasonal cycles in biomass burning and tropical deep convection [Schoeberl *et al.*, 2006,

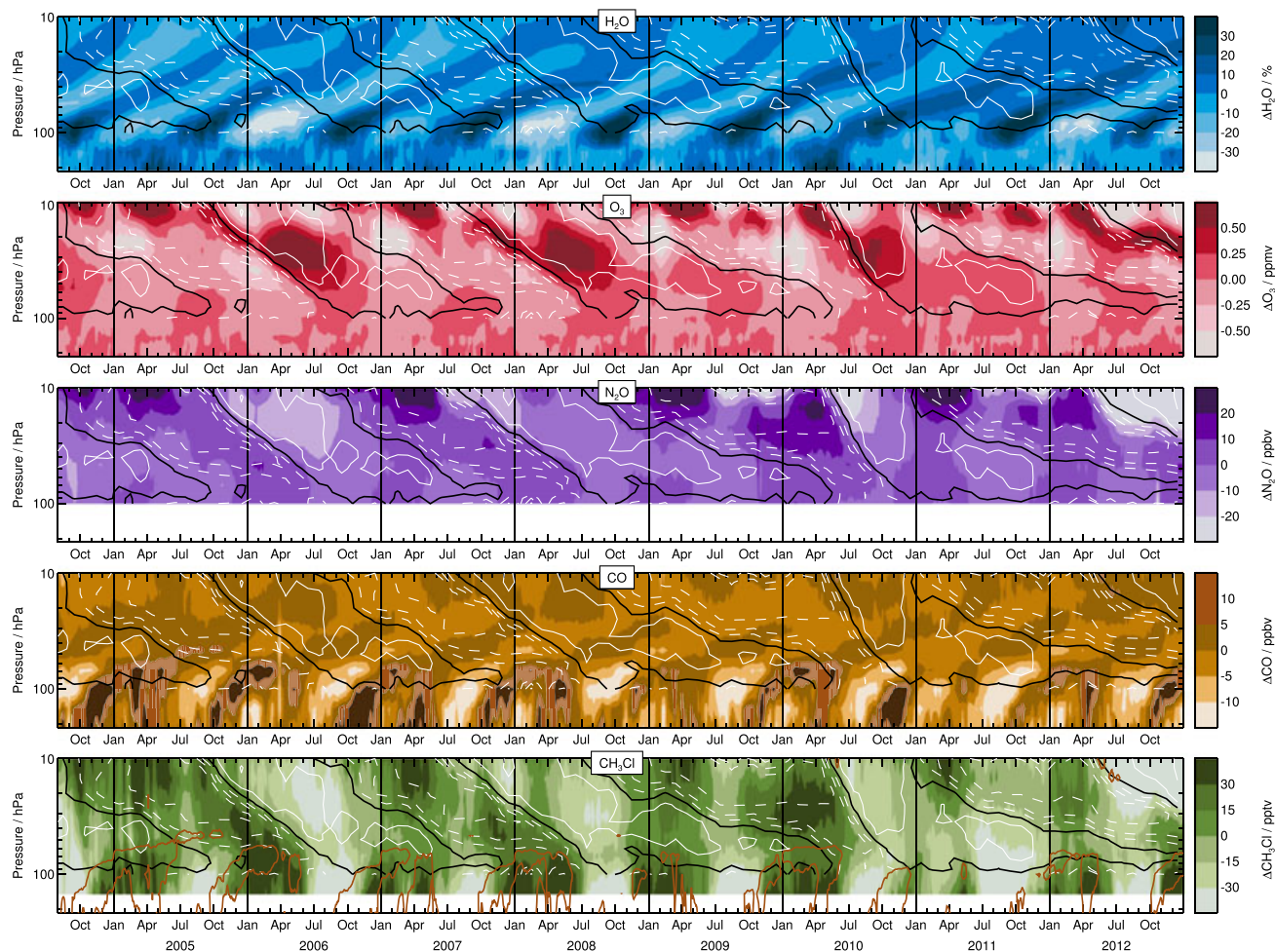


Figure 14. (top to bottom) Contour plots of MLS v3.3 H₂O, O₃, N₂O, CO, and CH₃Cl within $\pm 8^\circ$ of the equator as a function of pressure. All quantities are shown as absolute differences from the Aura mission mean, with the exception of H₂O, which is shown in terms of percent differences. The data have been smoothed slightly by running the daily averages through a Kalman smoother (as described by *Santee et al.* [2004]). Vertical black solid lines denote year boundaries. Overlays show monthly mean zonal winds (at 10 m/s intervals) at Singapore ($1^\circ\text{N}/104^\circ\text{E}$). Westerlies are shown as solid white contours, easterlies are shown as dashed white contours, and the zero wind line is depicted in black. On the CH₃Cl panel, the brown overlays represent the 5 ppbv contour of the CO anomaly to help guide the eye.

2008; *Liu et al.*, 2007]. *Pumphrey et al.* [2008] demonstrated that a tape recorder signal is detectable in MLS measurements of hydrogen cyanide (HCN), despite their poor vertical resolution (6–8 km over the altitude range 32–20 km). The irregular periodicity in the HCN tape recorder has been shown to be controlled mainly by interannual variations in biomass burning in Indonesia (strongly influenced by El Niño events, as discussed above) [*Pumphrey et al.*, 2008; *Li et al.*, 2009; *Pommrich et al.*, 2010; *Randel et al.*, 2010]. Given that CH₃Cl has vertical resolution comparable to that of CO and better than that of HCN (species in which a tape recorder has previously been discerned), it should also exhibit such a signature, although it must be borne in mind that the detailed vertical structure of the propagating features is inevitably attenuated by the relatively coarse MLS vertical resolution.

[62] To investigate the manifestation of tropical tape recorder and QBO signatures in CH₃Cl, in Figure 14 we

compare its seasonal cycle in a narrow band around the equator to those of several other products measured by MLS. All quantities are shown as differences from the Aura mission mean. The alternating bands of relatively wet and dry air rising from the tropical tropopause (Figure 14, first row) are hallmarks of the tape recorder effect. In contrast to H₂O, O₃ and N₂O (Figure 14, second and third rows, respectively) show little or no indication of a tape recorder, although they both display small annual oscillations at the lowest levels arising in part from fluctuations in the strength of the tropical upwelling in the Brewer-Dobson circulation [*Randel et al.*, 2007; *Schoeberl et al.*, 2008; *Abalos et al.*, 2012]. Horizontal transport from the extratropics has also been shown to make important contributions to the seasonal variations in O₃ and other species just above the tropical tropopause [*Konopka et al.*, 2010; *Santee et al.*, 2011; *Ploeger et al.*, 2012]. At higher altitudes, both O₃ and N₂O exhibit a pronounced QBO signal, with descending patterns of alternating high

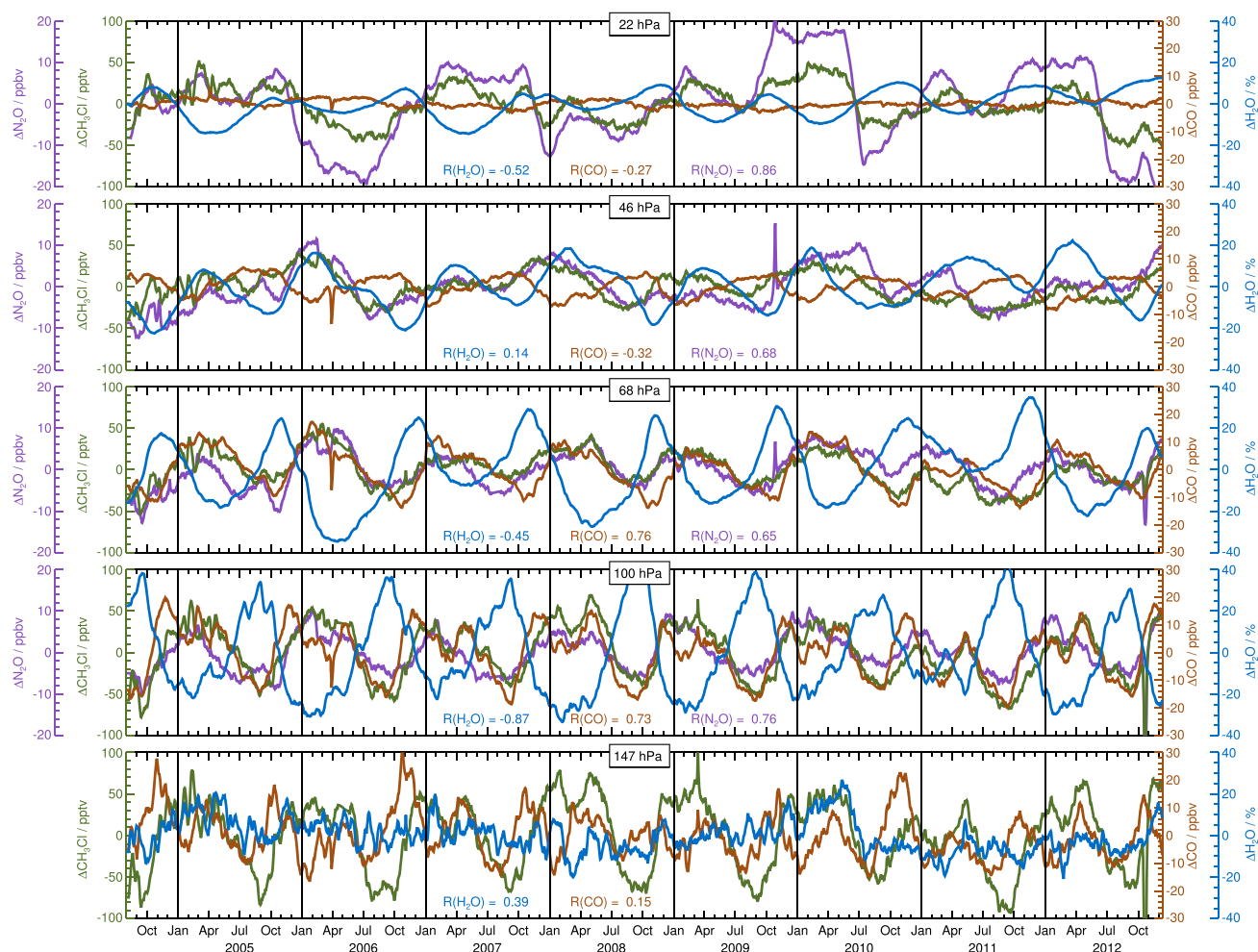


Figure 15. Time series of the H₂O (blue), CO (brown), N₂O (lavender), and CH₃Cl (green) anomalies (differences from Aura mission mean) at five pressure levels (22, 46, 68, 100, and 147 hPa). Note that a different y axis is used for each species. As in Figure 14, the anomalies have been smoothed slightly using a Kalman smoother. Correlation coefficients, R , quantifying the linear relationship between CH₃Cl and H₂O, CO, and N₂O (color coded by species) are also shown. Vertical black solid lines denote year boundaries.

and low values well correlated with the descent of the wind anomalies. Carbon monoxide (Figure 14, fourth row) is largely unaffected by either the QBO or in-mixing from mid-latitudes since its horizontal and vertical gradients are small above 20 km [Schoeberl *et al.*, 2008; Ploeger *et al.*, 2012]. It does, however, evince annual oscillations in the lower stratosphere that have both Brewer-Dobson [Randel *et al.*, 2007; Schoeberl *et al.*, 2008; Abalos *et al.*, 2012] and tape recorder components. Schoeberl *et al.* [2006] place the CO “tape head”, the altitude at which emerges the tape recorder pattern of sloping contours indicative of a phase lag with height, at between 360 and 375 K (which they estimated to lie between 147 and 100 hPa or 14 and 16 km). Because of its relatively short chemical lifetime (1–2 months), only traces of the CO tape recorder are discernible above \sim 20 km [Schoeberl *et al.*, 2006, 2008, see also Figure 14].

[63] The CH₃Cl field is characterized by greater vertical coherence than the other species (Figure 14, fifth row). This degree of uniformity in its distribution over such a large vertical range is well beyond what could be explained

by the relatively coarse vertical resolution of the MLS CH₃Cl measurements and possibly reflects a combination of quasi-biennial and annual oscillation effects. Downward-propagating anomalies at the higher levels parallel the pattern in N₂O (and the obverse in O₃) fairly closely. This apparent QBO signal merges with an annual cycle at the lower levels that echoes the variations seen in CO. Comparison of the behavior of CH₃Cl with that of CO shows that the timing and magnitude of the variations in the two species are similar, as is the upward tilt of the contour lines and thus the phase lag with altitude indicative of a tape recorder-like effect. As for CO, the tape recorder signal in CH₃Cl likely arises in large measure from the seasonal cycles in its sources and convection. The altitude above which the CH₃Cl tape recorder signal fades out is difficult to identify definitively because the clear QBO signal begins to dominate, but it is expected to be higher than for CO because of the longer lifetime of CH₃Cl.

[64] Time series of the anomalies in several species are shown for various pressure levels in Figure 15. These

Table 2. Summary of Aura MLS v3.3 CH₃Cl Characteristics

Pressure (hPa)	Resolution Vertical × Horizontal ^a (km)	Precision ^b (pptv)	Systematic Uncertainty (%)
15–4.6	7–10 × 550–850	±100	30–75
100–22	4–6 × 450–500	±100	30–45
147	4.5 × 600	±100	45

^aHorizontal resolution in the direction along the measurement track.

^bPrecision on individual profiles.

“slices” through the temporal evolution demonstrate a strong positive correlation between CH₃Cl and N₂O at all altitudes. At 22 and 46 hPa, this high degree of correspondence, together with the relatively weak relationship with CO, is consistent with a QBO signature in the CH₃Cl variations. At 68 and 100 hPa, CH₃Cl is strongly correlated with CO and anticorrelated with H₂O, consistent with a tape recorder effect. That the correlation with N₂O is also strong at these levels, however, suggests that variations in the Brewer-Dobson circulation also significantly influence tropical CH₃Cl variability. Thus, like CO, CH₃Cl appears to be controlled by both variations in tropical upwelling and forcing by a tape recorder signal. The semiannual cycle that is present in CO at 100 and 147 hPa, with a characteristic double-peak structure arising from the seasonal cycles in biomass burning and convection [Schoeberl *et al.*, 2006; Liu *et al.*, 2007; Randel *et al.*, 2007; Abalos *et al.*, 2012], is not as clearly visible in the CH₃Cl at those levels in most years. The periodicity in the CH₃Cl cycle may be more irregular, as is the case for HCN as mentioned earlier, and biogenic processes also play a greater role. More detailed investigation of the mechanisms responsible for the variability in tropical CH₃Cl abundances will be the subject of future studies.

5. Summary, Synthesis, and Next Steps

[65] Methyl chloride, the most abundant chlorine compound in the troposphere, is simultaneously produced and consumed by the terrestrial biosphere. Because of its large fluxes into the atmosphere and moderately long lifetime (1–1.2 years in the global average), significant amounts of CH₃Cl are transported into the stratosphere, where it constitutes by far the largest natural source of ozone-destroying chlorine radicals. Its importance in stratospheric ozone chemistry is expected to increase in the future as emission controls alter the relative contributions from natural and anthropogenic halogen sources. Changes in climate and land use patterns may also influence CH₃Cl production and degradation and thus the fluxes to and uptake from the atmosphere. Therefore, a quantitative understanding of the CH₃Cl distribution and variability will help enhance our predictive capability for ozone layer stability.

[66] Aura MLS provides the first daily global observations of CH₃Cl. Retrieval of CH₃Cl was undertaken as part of the development of the MLS v3.3 data processing algorithms because emission from CH₃Cl lines in the 640 GHz band was found to be partially responsible for the substantial negative bias present at the lowest retrieval levels in earlier versions of the MLS ClO data. The retrieval of CH₃Cl in the v3.3 algorithms yielded not only a greatly improved ClO product, but also a reliable measurement of CH₃Cl.

[67] Here we report the results of various validation exercises that confirm the quality of the v3.3 MLS CH₃Cl data

and their usefulness for scientific studies. The estimated vertical and horizontal resolution of the v3.3 MLS CH₃Cl data over their recommended vertical range is summarized in Table 2. Although overlap in the averaging kernels for the 100 and 147 hPa retrieval surfaces indicates that the 147 hPa retrievals do not provide completely independent information, they display significant spatial and temporal variations (not all of which are present at 100 hPa) that appear to faithfully reflect real atmospheric features. The precision and systematic uncertainty of the v3.3 MLS CH₃Cl data are also given in Table 2. The overall uncertainty (in pptv) for an individual CH₃Cl data point is determined by taking the RSS of the precision and systematic uncertainty terms (note that the latter, expressed as a scaling error, depends on the measured mixing ratio at that point); for averages, the single-profile precision value is divided by the square root of the number of profiles contributing to the average.

[68] Extensive comparisons with correlative CH₃Cl measurements, in particular from ACE-FTS, have been shown. Although a latitudinally and temporally varying offset is present between the MLS and ACE-FTS CH₃Cl data sets, they exhibit very similar seasonal oscillations and geographical gradients. In addition, the MLS and ACE-FTS CH₃Cl/CO relationships in the UTLS agree very well.

[69] Quality control should be implemented in any scientific studies using the MLS CH₃Cl measurements. Several diagnostics for evaluating data quality are provided along with the retrieved mixing ratios in the MLS Level 2 files. Briefly, CH₃Cl data points for which any of the following conditions are met should be discarded: (1) the associated precision value is negative, (2) “Status” has a nonzero value (at least for pressures greater than or equal to 68 hPa; at lower pressures, cloud effects are minimal, and data points with nonzero but even values of Status may be used), (3) “Quality” is less than 1.3, or (4) “Convergence” is greater than 1.05.

[70] We have exploited the unparalleled scope of the global long-term (spanning more than 8 years at the time of writing) MLS data set to investigate spatial and temporal variations in the distribution of CH₃Cl in the upper troposphere and stratosphere. We present here the first global climatology of CH₃Cl and compare its behavior to that observed in other species measured by MLS. Such a comprehensive description of the CH₃Cl distribution in the tropopause region and stratosphere provides global and seasonal context for the sparse aircraft and balloon profiling of CH₃Cl that has been performed in the UTLS over the years, supplies information that may be useful for model initialization and validation purposes, and represents a valuable baseline against which the future CH₃Cl burden may be assessed.

[71] As is the case for CO, the distribution of CH₃Cl near the tropopause is controlled by the complex interplay between surface emissions, convection, and long-range hor-

horizontal transport. Both species are markers of pollution from biomass burning that can be lofted to the UTLS very rapidly by deep convection or other fast processes. Seasonal variations in regional fire activity and other surface sources as well as in the frequency, strength, and location of convective updrafts lead to climatological “hot spots” in CH₃Cl in the upper troposphere over Africa and South America. In addition, persistent enhancements occur over the entire southern Asian region during summer of every year, as pollution transported upward by deep convection over the monsoon region and Tibetan Plateau becomes trapped within the monsoon anticyclone in the UTLS. Apart from these annually recurring patterns, anomalously strong enhancements and depressions in tropical upper tropospheric CH₃Cl have been linked to specific events in some years. For example, appreciable enhancements in upper tropospheric CH₃Cl in the vicinity of Indonesia in October and November 2006 reflect increased emissions from large-scale forest fires induced by a moderate El Niño in that year. Over South America, larger abundances of CH₃Cl are associated with particularly severe fire seasons in 2004, 2005, and 2010, although the intense burning in this region in 2007 apparently caused enhancements in CO but not in CH₃Cl. In contrast, smaller emissions in the low-fire years of 2006, 2008, and 2009 resulted in depressed CH₃Cl abundances over South America. An extreme enhancement in upper tropospheric CH₃Cl over central Africa in February 2005, the largest in the MLS record for this region and season, is related to high fire emissions and unusually vigorous vertical mixing. In other cases (e.g., over much of the African continent in May 2005), substantially suppressed CH₃Cl mixing ratios stem from a combination of little fire pollution and weak convective activity. Upper tropospheric CH₃Cl and CO concentrations are considerably lower than the climatological values over much of the tropics and subtropics throughout 2011; it is possible that below-average biomass burning activity in South America had near-global impact on upper tropospheric trace gas abundances that year.

[72] In addition to its utility for tracking the lofting of pollution by deep convection, CH₃Cl is valuable as a tracer of large-scale transport and mixing processes. In general, its behavior is tightly correlated with that of N₂O. Both data products have comparable vertical resolution in the UTLS; the CH₃Cl measurements have poorer precision, but because MLS N₂O data are not recommended for scientific studies at pressures greater than 100 hPa, MLS CH₃Cl is a more useful tracer of air motions in the upper troposphere and lowermost stratosphere. Confined diabatic descent inside the stratospheric polar vortices brings down air poor in CH₃Cl from above, producing a pronounced minimum in CH₃Cl in these regions in the winter and spring in both hemispheres. Outflow from the decaying vortex in spring is manifested by the equatorward spread of low CH₃Cl abundances. Quasi-horizontal cross-tropopause transport and mixing also play a major role in governing the CH₃Cl distribution, especially at 370 K, where evidence of both stratosphere-to-troposphere and troposphere-to-stratosphere transport events associated with the summer monsoon circulations can be seen. Distinctly enhanced wintertime transport of CH₃Cl from the tropics to high southern latitudes observed at 850 K during phases in which equatorial winds are easterly is a signature of the QBO. Anomalous poleward transport of lower-

latitude air in the Southern Hemisphere middle stratosphere was induced by an unusually strong minor stratospheric sudden warming that developed midway through the 2010 Antarctic winter. Although the CH₃Cl data are relatively noisy, unambiguous descending patterns of alternating high and low values in the middle stratosphere parallel the behavior seen in other species measured by MLS, such as N₂O and O₃; this QBO signal then merges with a less well-defined annual cycle at lower altitudes. Similar to the tape recorder-like effect previously reported in CO, these variations likely arise from the seasonal cycles in the CH₃Cl sources (in particular biomass burning) and convection. The results shown in this work illustrate how the lifetimes and spatial gradients of different species interact with changes in their emissions, ascent rates, and other atmospheric variations such as the QBO to control their distributions in the UTLS. Making simultaneous measurements of multiple species thus provides more stringent constraints on the provenance and dynamical history of sampled air parcels and is extremely valuable for teasing out which processes dominate for a given species.

[73] In general, measurements of the spatial and temporal variations of a relatively long-lived species of tropospheric origin such as CH₃Cl are of great value for investigating troposphere-stratosphere exchange processes and their representation in models. For example, *Ricaud et al.* [2007] compared satellite observations of several tropospheric tracers with dissimilar sources and lifetimes to simulations from a three-dimensional chemical transport model in order to assess the relative importance of various processes in regulating trace gas abundances in the UTLS. In future work, we plan to investigate in detail the relative roles of surface emissions (location, magnitude, and seasonality), vertical and horizontal transport, and convection in governing trace gas distributions in the tropopause region and lower stratosphere. Since neither the geographical distribution nor the magnitude of CH₃Cl sources has yet been fully resolved, any additional constraints provided by the daily global MLS measurements would be invaluable.

[74] **Acknowledgments.** We thank Ryan Fuller, William Daffer, Bob Thurstans, Brian Knosp, and Brian Mills for programming, system administration, and data management support. We gratefully acknowledge provision of MkIV data by Geoffrey Toon and the MkIV Team, ACE-FTS data by Kaley Walker and the ACE-FTS Team, and Singapore winds by the Institute of Meteorology of the Freie Universität Berlin. Comments from three anonymous reviewers substantially improved the manuscript. Work at the Jet Propulsion Laboratory, California Institute of Technology, was done under contract with the National Aeronautics and Space Administration.

References

- Abalos, M., W. J. Randel, and E. Serrano (2012), Variability in upwelling across the tropical tropopause and correlations with tracers in the lower stratosphere, *Atmos. Chem. Phys.*, *12*, 11,505–11,517.
- Andreae, M. O., and P. Merlet (2001), Emission of trace gases and aerosols from biomass burning, *Global Biogeochem. Cycles*, *15*, 955–966.
- Andreae, M. O., et al. (1996), Methyl halide emissions from savanna fires in southern Africa, *J. Geophys. Res.*, *101*, 23,603–23,613.
- Avallone, L. M., and M. J. Prather (1997), Tracer-tracer correlations: Three-dimensional model simulations and comparisons to observations, *J. Geophys. Res.*, *102*, 19,233–19,246.
- Aydin, M., E. S. Saltzman, W. J. D. Bruyn, S. A. Montzka, J. H. Butler, and M. Battle (2004), Atmospheric variability of methyl chloride during the last 300 years from an Antarctic ice core and firn air, *Geophys. Res. Lett.*, *31*, L02109, doi:10.1029/2003GL018750.

- Baldwin, M. P., and T. J. Dunkerton (1998), Quasi-biennial modulation of the Southern Hemisphere stratospheric polar vortex, *Geophys. Res. Lett.*, *25*, 3343–3346.
- Baldwin, M. P., et al. (2001), The quasi-biennial oscillation, *Rev. Geophys.*, *39*, 179–229.
- Barret, B., et al. (2008), Transport pathways of CO in the African upper troposphere during the monsoon season: A study based upon the assimilation of spaceborne observations, *Atmos. Chem. Phys.*, *8*, 3231–3246.
- Bernath, P. F., et al. (2005), Atmospheric chemistry experiment (ACE): Mission overview, *Geophys. Res. Lett.*, *32*, L15S01, doi:10.1029/2005GL022386.
- Blake, N. J., D. R. Blake, B. C. Sive, T.-Y. Chen, F. S. Rowland, J. E. Collins, G. W. Sachse, and B. E. Anderson (1996), Biomass burning emissions and vertical distribution of atmospheric methyl halides and other reduced carbon gases in the South Atlantic region, *J. Geophys. Res.*, *101*, 24,151–24,164.
- Blake, N. J., D. R. Blake, T.-Y. Chen, J. E. Collins, G. W. Sachse, B. E. Anderson, and F. S. Rowland (1997), Distribution and seasonality of selected hydrocarbons and halocarbons over the western Pacific basin during PEM-West A and PEM-West B, *J. Geophys. Res.*, *102*, 28,315–28,331.
- Blake, N. J., et al. (2001), Large-scale latitudinal and vertical distributions of NMHCs and selected halocarbons in the troposphere over the Pacific Ocean during the March–April 1999 Pacific Exploratory Mission (PEM-Tropics B), *J. Geophys. Res.*, *106*, 32,627–32,644.
- Blake, N. J., et al. (2003), NMHCs and halocarbons in Asian continental outflow during the Transport and Chemical Evolution over the Pacific (TRACE-P) field campaign: Comparison with PEM-West B, *J. Geophys. Res.*, *108*, 8806, doi:10.1029/2002JD003367.
- Blei, E., C. J. Hardacre, G. P. Mills, K. V. Heal, and M. R. Heal (2010), Identification and quantification of methyl halide sources in a lowland tropical rainforest, *Atmos. Environ.*, *44*, 1005–1010.
- Boone, C. D., R. Nassar, K. A. Walker, Y. Rochon, S. D. McLeod, C. P. Rinsland, and P. F. Bernath (2005), Retrievals for the atmospheric chemistry experiment Fourier-transform spectrometer, *Appl. Opt.*, *44*, 7218–7231.
- Brown, A. T., M. P. Chipperfield, C. Boone, C. Wilson, K. A. Walker, and P. F. Bernath (2011), Trends in atmospheric halogen containing gases since 2004, *J. Quant. Spectrosc. Radiat. Transfer*, *112*, 2552–2566.
- Butchart, N., and E. E. Remsburg (1986), The area of the stratospheric polar vortex as a diagnostic for tracer transport on an isentropic surface, *J. Atmos. Sci.*, *43*, 1319–1339.
- Butler, J. H. (2000), Better budgets for methyl halides?, *Nature*, *403*, 260–261.
- Butler, J. H., et al. (1999), A record of atmospheric halocarbons during the twentieth century from polar firn air, *Nature*, *399*, 749–755.
- Chandra, S., J. R. Ziemke, M. R. Schoeberl, L. Froidevaux, W. G. Read, P. F. Levelt, and P. K. Bhartia (2007), Effects of the 2004 El Niño on tropospheric ozone and water vapor, *Geophys. Res. Lett.*, *34*, L06802, doi:10.1029/2006GL028779.
- Chandra, S., J. R. Ziemke, B. N. Duncan, T. L. Diehl, N. J. Livesey, and L. Froidevaux (2009), Effects of the 2006 El Niño on tropospheric ozone and carbon monoxide: Implications for dynamics and biomass burning, *Atmos. Chem. Phys.*, *9*, 4239–4249.
- Chen, Y., J. T. Randerson, D. C. Morton, R. S. DeFries, G. J. Collatz, P. S. Kasibhatla, L. Giglio, Y. Jin, and M. E. Marlier (2011), Forecasting fire season severity in South America using sea surface temperature anomalies, *Science*, *334*, 787–791.
- Chipperfield, M. P., and L. J. Gray (1992), Two-dimensional model studies of the interannual variability of trace gases in the middle atmosphere, *J. Geophys. Res.*, *97*, 5963–5980.
- Ciais, P., et al. (2005), Europe-wide reduction in primary productivity caused by the heat and drought in 2003, *Nature*, *437*, 529–533.
- Cicerone, R. J., D. H. Stedman, and R. S. Stolarski (1975), Estimate of late 1974 stratospheric concentration of gaseous chlorine compounds (ClX), *Geophys. Res. Lett.*, *2*, 219–222.
- Cox, M. L., G. A. Sturrock, P. J. Fraser, S. T. Siems, P. B. Krummel, and S. O'Doherty (2003), Regional sources of methyl chloride, chloroform and dichloromethane identified from AGAGE observations at Cape Grim, Tasmania, 1998–2000, *J. Atmos. Chem.*, *45*, 79–99.
- Cramb, R., and G. N. Curry (2012), Oil palm and rural livelihoods in the Asia-Pacific region: An overview, *Asia Pac. Viewp.*, *53*, 223–239.
- Cronn, D. R., and W. Nutmagul (1982), Characterization of trace gases in 1980 volcanic plumes of Mt. St. Helens, *J. Geophys. Res.*, *87*, 11,153–11,160.
- Cronn, D. R., R. A. Rasmussen, E. Robinson, and D. E. Harsch (1977), Halogenated compound identification and measurement in the troposphere and lower stratosphere, *J. Geophys. Res.*, *82*, 5935–5944.
- Crutzen, P. J., and M. O. Andreae (1990), Biomass burning in the tropics: Impact on atmospheric chemistry and biogeochemical cycles, *Science*, *250*, 1669–1678.
- Crutzen, P. J., and L. T. Gidel (1983), A two-dimensional photochemical model of the atmosphere, 2: The tropospheric budgets of the anthropogenic chlorocarbons CO, CH₄, CH₃Cl and the effect of various NO_x sources on tropospheric ozone, *J. Geophys. Res.*, *88*, 6641–6661.
- Crutzen, P. J., L. E. Heidt, J. P. Krasnec, W. H. Pollock, and W. Seiler (1979), Biomass burning as a source of atmospheric gases CO, H₂, N₂O, NO, CH₃Cl, and COS, *Nature*, *282*, 253–256.
- de Laat, A. T. J., and M. van Weele (2011), The 2010 Antarctic ozone hole: Observed reduction in ozone destruction by minor sudden stratospheric warmings, *Sci. Rep.*, *1*, 38, doi:10.1038/srep00038.
- Dimmer, C. H., P. G. Simmonds, G. Nickless, and M. R. Bassford (2001), Biogenic fluxes of halomethanes from Irish peatland ecosystems, *Atmos. Environ.*, *35*, 321–330.
- Duncan, B. N., R. V. Martin, A. C. Staudt, R. Yevich, and J. A. Logan (2003), Interannual and seasonal variability of biomass burning emissions constrained by satellite observations, *J. Geophys. Res.*, *108*(D2), 4100, doi:10.1029/2002JD002378.
- Duncan, B. N., S. E. Strahan, Y. Yoshida, S. D. Steenrod, and N. Livesey (2007), Model study of the cross-tropopause transport of biomass burning pollution, *Atmos. Chem. Phys.*, *7*, 3713–3736.
- Fabian, P., R. Borchers, S. A. Penkett, and N. J. D. Prosser (1981), Halocarbons in the stratosphere, *Nature*, *294*, 733–735.
- Fabian, P., R. Borchers, R. Leifer, B. H. Subbaraya, S. Lal, and M. Boy (1996), Global stratospheric distribution of halocarbons, *Atmos. Environ.*, *30*, 1787–1796.
- Fischer, H., et al. (2002), Synoptic tracer gradients in the upper troposphere over central Canada during the Stratosphere-Troposphere Experiments by Aircraft Measurements 1998 summer campaign, *J. Geophys. Res.*, *107*(D8), 4064, doi:10.1029/2000JD000312.
- Froidevaux, L., et al. (2008), Validation of Aura Microwave Limb Sounder stratospheric ozone measurements, *J. Geophys. Res.*, *113*, D15S20, doi:10.1029/2007JD008771.
- Fu, R., Y. Hu, J. S. Wright, J. H. Jiang, R. E. Dickinson, M. Chen, M. Filipiak, W. G. Read, J. W. Waters, and D. L. Wu (2006), Short circuit of water vapor and polluted air to the global stratosphere by convective transport over the Tibetan Plateau, *Proc. Natl. Acad. Sci. U.S.A.*, *103*, 5664–5669.
- Garny, H., G. E. Bodeker, and M. Dameris (2007), Trends and variability in stratospheric mixing: 1979–2005, *Atmos. Chem. Phys.*, *7*, 5611–5624.
- Gerlach, T. M. (1980), Evaluation of volcanic gas analyses from Kilauea volcano, *J. Volcanol. Geotherm. Res.*, *7*, 295–317.
- Graedel, T. E., and W. C. Keene (1995), Tropospheric budget of reactive chlorine, *Global Biogeochem. Cycles*, *9*, 47–77.
- Grimsrud, E. P., and R. A. Rasmussen (1975), Survey and analysis of halocarbons in the atmosphere by gas chromatography-mass spectrometry, *Atmos. Environ.*, *9*, 1014–1017.
- Hamilton, J. T. G., W. C. McRoberts, F. Keppler, R. M. Kalin, and D. B. Harper (2003), Chloride methylation by plant pectin: An efficient environmentally significant process, *Science*, *301*, 206–209.
- Hardacre, C. J., E. Blei, and M. R. Heal (2009), Growing season methyl bromide and methyl chloride fluxes at a sub-Arctic wetland in Sweden, *Geophys. Res. Lett.*, *36*, L12401, doi:10.1029/2009GL038277.
- Harper, D. B. (1985), Halomethane from halide ion: A highly efficient fungal conversion of environmental significance, *Nature*, *315*, 55–57.
- Haynes, P., and E. Shuckburgh (2000), Effective diffusivity as a diagnostic of atmospheric transport, 2. Troposphere and lower stratosphere, *J. Geophys. Res.*, *105*, 22,795–22,810.
- Hu, L., S. Yvon-Lewis, Y. Liu, J. E. Salisbury, and J. E. O'Hern (2010), Coastal emissions of methyl bromide and methyl chloride along the eastern Gulf of Mexico and the east coast of the United States, *Global Biogeochem. Cycles*, *24*, GB1007, doi:10.1029/2009GB003514.
- Hu, L., S. A. Yvon-Lewis, J. H. Butler, J. M. Lobert, and D. B. King (2013), An improved oceanic budget for methyl chloride, *J. Geophys. Res. Oceans*, *118*, 715–725, doi:10.1029/2012JC008196.
- Inn, E. C. Y., J. F. Vedder, E. P. Condon, and D. O'Hara (1981), Gaseous constituents in the plume from eruptions of Mount St. Helens, *Science*, *211*, 821–823.
- Jiang, J. H., N. J. Livesey, H. Su, L. Neary, J. C. McConnell, and N. A. D. Richards (2007), Connecting surface emissions, convective uplifting, and long-range transport of carbon monoxide in the upper troposphere: New observations from the Aura Microwave Limb Sounder, *Geophys. Res. Lett.*, *34*, L18812, doi:10.1029/2007GL030638.
- Kaspers, K. A., et al. (2004), Analyses of firm gas samples from Dronning Maud Land, Antarctica: Study of nonmethane hydrocarbons and methyl chloride, *J. Geophys. Res.*, *109*, D02307, doi:10.1029/2003JD003950.

- Keene, W. C., et al. (1999), Composite global emissions of reactive chlorine from anthropogenic and natural sources: Reactive Chlorine Emissions Inventory, *J. Geophys. Res.*, *104*, 8429–8440.
- Keppler, F., R. Eiden, V. Niedan, J. Pracht, and H. F. Schöler (2000), Halocarbons produced by natural oxidation processes during degradation of organic matter, *Nature*, *403*, 298–301.
- Keppler, F., D. B. Harper, T. Röckmann, R. M. Moore, and J. T. G. Hamilton (2005), New insight into the atmospheric chloromethane budget gained using stable carbon isotope ratios, *Atmos. Chem. Phys.*, *5*, 2403–2411.
- Khalil, M. A. K., and R. A. Rasmussen (1999), Atmospheric methyl chloride, *Atmos. Environ.*, *33*, 1305–1321.
- Khalil, M. A. K., and R. A. Rasmussen (2000), Soil-atmosphere exchange of radiatively and chemically active gases, *Environ. Sci. Pollut. Res. Int.*, *7*, 79–82.
- Khalil, M. A. K., R. M. Moore, D. B. Harper, J. M. Lobert, D. J. Erickson, V. Koropalov, W. T. Sturges, and W. C. Keene (1999), Natural emissions of chlorine-containing gases: Reactive Chlorine Emissions Inventory, *J. Geophys. Res.*, *104*, 8333–8346.
- Klekociuk, A. R., et al. (2011), The Antarctic ozone hole during 2010, *Aust. Met. Oceanogr. J.*, *61*, 253–267.
- Konopka, P., J.-U. Groöf, G. Günther, F. Ploeger, R. Pommrich, R. Müller, and N. Livesey (2010), Annual cycle of ozone at and above the tropical tropopause: Observations versus simulations with the Chemical Lagrangian Model of the Stratosphere (CLaMS), *Atmos. Chem. Phys.*, *10*, 121–132.
- Kuttippurath, J., and G. Nikulin (2012), A comparative study of the major sudden stratospheric warmings in the Arctic winters 2003/2004–2009/2010, *Atmos. Chem. Phys.*, *12*, 8115–8129.
- Labitzke, K., and M. Kunze (2009), On the remarkable Arctic winter in 2008/2009, *J. Geophys. Res.*, *114*, D00102, doi:10.1029/2009JD012273.
- Lambert, A., et al. (2007), Validation of the Aura Microwave Limb Sounder middle atmosphere water vapor and nitrous oxide measurements, *J. Geophys. Res.*, *112*, D24S36, doi:10.1029/2007JD008724.
- Lee, J. N., D. L. Wu, G. L. Manney, M. J. Schwartz, A. Lambert, N. J. Livesey, K. R. Minschwaner, H. C. Pumphrey, and W. G. Read (2011), Aura Microwave Limb Sounder observations of the polar middle atmosphere: Dynamics and transport of CO and H₂O, *J. Geophys. Res.*, *116*, D05110, doi:10.1029/2010JD014608.
- Lee-Taylor, J. M., G. P. Brasseur, and Y. Yokouchi (2001), A preliminary three-dimensional global model study of atmospheric methyl chloride distributions, *J. Geophys. Res.*, *106*, 34,221–34,233.
- Li, Q., P. I. Palmer, H. C. Pumphrey, P. Bernath, and E. Mahieu (2009), What drives the observed variability of HCN in the troposphere and lower stratosphere?, *Atmos. Chem. Phys.*, *9*, 8531–8543.
- Li, Q., et al. (2005), Convective outflow of South Asian pollution: A global CTM simulation compared with EOS MLS observations, *Geophys. Res. Lett.*, *32*, L14826, doi:10.1029/2005GL022762.
- Liu, C., E. J. Zipser, T. Garrett, J. H. Jiang, and H. Su (2007), How do the water vapor and carbon monoxide ‘tape recorders’ start near the tropical tropopause?, *Geophys. Res. Lett.*, *34*, L09804, doi:10.1029/2006GL029234.
- Liu, J., J. A. Logan, D. B. A. Jones, N. J. Livesey, I. Megretskaja, C. Carouge, and P. Nedelec (2010), Analysis of CO in the tropical troposphere using Aura satellite data and the GEOS-Chem model: Insights into transport characteristics of the GEOS meteorological products, *Atmos. Chem. Phys.*, *10*, 12,207–12,232.
- Livesey, N. J., M. D. Fromm, J. W. Waters, G. L. Manney, M. L. Santee, and W. G. Read (2004), Enhancements in lower stratospheric CH₃CN observed by the Upper Atmosphere Research Satellite Microwave Limb Sounder following boreal forest fires, *J. Geophys. Res.*, *109*, D06308, doi:10.1029/2003JD004055.
- Livesey, N. J., W. V. Snyder, W. G. Read, and P. A. Wagner (2006), Retrieval algorithms for the EOS microwave limb sounder (MLS), *IEEE Trans. Geosci. Remote Sens.*, *44*, 1144–1155.
- Livesey, N. J., J. A. Logan, M. L. Santee, J. W. Waters, R. M. Doherty, W. G. Read, L. Froidevaux, and J. H. Jiang (2013a), Interrelated variations of O₃, CO and deep convection in the tropical/subtropical upper troposphere observed by the Aura Microwave Limb Sounder (MLS) during 2004–2011, *Atmos. Chem. Phys.*, *13*, 579–598.
- Livesey, N. J., et al. (2008a), Validation of Aura Microwave Limb Sounder O₃ and CO observations in the upper troposphere and lower stratosphere, *J. Geophys. Res.*, *112*, D15S02, doi:10.1029/2007JD008805.
- Livesey, N. J., et al., (2008b), Version 2.2 Level 2 data quality and description document, Jet Propulsion Laboratory, Pasadena, California, available from <http://mlls.jpl.nasa.gov>.
- Livesey, N. J., et al., (2013b), Version 3.3 and 3.4 Level 2 data quality and description document, Jet Propulsion Laboratory, Pasadena, California, available from <http://mlls.jpl.nasa.gov>.
- Lobert, J. M., W. C. Keene, J. A. Logan, and R. Yevich (1999), Global chlorine emissions from biomass burning: Reactive Chlorine Emissions Inventory, *J. Geophys. Res.*, *104*, 8373–8389.
- Logan, J. A., I. Megretskaja, R. Nassar, L. T. Murray, L. Zhang, K. W. Bowman, H. M. Worden, and M. Luo (2008), Effects of the 2006 El Niño on tropospheric composition as revealed by data from the Tropospheric Emission Spectrometer (TES), *Geophys. Res. Lett.*, *35*, L03816, doi:10.1029/2007GL031698.
- Lovelock, J. E. (1975), Natural halocarbons in the air and in the sea, *Nature*, *256*, 193–194.
- Manley, S. L., N.-Y. Wang, M. L. Walser, and R. J. Cicerone (2007), Methyl halide emissions from greenhouse-grown mangroves, *Geophys. Res. Lett.*, *34*, L01806, doi:10.1029/2006GL027777.
- Manney, G. L., R. W. Zurek, A. O’Neill, and R. Swinbank (1994), On the motion of air through the stratospheric polar vortex, *J. Atmos. Sci.*, *51*, 2973–2994.
- Manney, G. L., M. J. Schwartz, K. Krüger, M. L. Santee, S. Pawson, J. N. Lee, W. H. Daffer, R. A. Fuller, and N. J. Livesey (2009a), Aura Microwave Limb Sounder observations of dynamics and transport during the record-breaking 2009 Arctic stratospheric major warming, *Geophys. Res. Lett.*, *36*, L12815, doi:10.1029/2009GL038586.
- Manney, G. L., et al. (2009b), Satellite observations and modeling of transport in the upper troposphere through the lower mesosphere during the 2006 major stratospheric sudden warming, *Atmos. Chem. Phys.*, *9*, 4775–4795.
- Manney, G. L., et al. (2011), Jet characterization in the upper troposphere/lower stratosphere (UTLS): Applications to climatology and transport studies, *Atmos. Chem. Phys.*, *11*, 6115–6137.
- Marcy, T. P., et al. (2007), Measurements of trace gases in the tropical tropopause layer, *Atmos. Environ.*, *41*, 7253–7261.
- McAnulla, C., I. R. McDonald, and J. C. Murrell (2001), Methyl chloride utilising bacteria are ubiquitous in the natural environment, *FEMS Microbiol. Lett.*, *201*, 151–155.
- McCulloch, A., M. L. Aucott, C. M. Benkovitz, T. E. Graedel, G. Kleiman, P. M. Midgley, and Y.-F. Li (1999), Global emissions of hydrogen chloride and chloromethane from coal combustion, incineration and industrial activities: Reactive Chlorine Emissions Inventory, *J. Geophys. Res.*, *104*, 8391–8403.
- Mead, M. I., M. A. H. Khan, G. Nickless, B. R. Grealley, D. Tainton, T. Pitman, and D. E. Shallcross (2008), Leaf cutter ants: A possible missing source of biogenic halocarbons, *Environ. Chem.*, *5*, 5–10, doi:10.1071/EN07068.
- Montzka, S. A., J. H. Butler, R. C. Myers, T. M. Thompson, T. H. Swanson, A. D. Clarke, L. T. Lock, and J. W. Elkins (1996), Decline in the tropospheric abundance of halogen from halocarbons: Implications for stratospheric ozone depletion, *Science*, *272*, 1318–1322.
- Moore, R. M., W. Groszko, and S. J. Niven (1996), Ocean-atmosphere exchange of methyl chloride: Results from NW Atlantic and Pacific Ocean studies, *J. Geophys. Res.*, *101*, 28,529–28,538.
- Moore, R. M., A. Gut, and M. O. Andreae (2005), A pilot study of methyl chloride emissions from tropical woodrot fungi, *Chemosphere*, *58*, 221–225.
- Mote, P. W., K. H. Rosenlof, M. E. McIntyre, E. S. Carr, J. C. Gille, J. R. Holton, J. S. Kinnerson, H. C. Pumphrey, J. M. Russell, and J. W. Waters (1996), An atmospheric tape recorder: The imprint of tropical tropopause temperatures on stratospheric water vapor, *J. Geophys. Res.*, *101*, 3989–4006.
- Nassar, R., J. A. Logan, I. A. Megretskaja, L. T. Murray, L. Zhang, and D. B. A. Jones (2009), Analysis of tropical tropospheric ozone, carbon monoxide, and water vapor during the 2006 El Niño using TES observations and the GEOS-Chem model, *J. Geophys. Res.*, *114*, D17304, doi:10.1029/2009JD011760.
- Nassar, R., et al. (2006), A global inventory of stratospheric chlorine in 2004, *J. Geophys. Res.*, *111*, D22312, doi:10.1029/2006JD007073.
- Naujokat, B. (1986), An update of the observed quasi-biennial oscillation of the stratospheric winds over the tropics, *J. Atmos. Sci.*, *43*, 1873–1877.
- Park, J. H., R. Zander, C. B. Farmer, C. P. Rinsland, J. M. Russell, R. H. Norton, and O. F. Raper (1986), Spectroscopic detection of CH₃Cl in the upper troposphere and lower stratosphere, *Geophys. Res. Lett.*, *13*, 765–768.
- Park, M., W. J. Randel, A. Gettelman, S. T. Massie, and J. H. Jiang (2007), Transport above the Asian summer monsoon anticyclone inferred from Aura Microwave Limb Sounder tracers, *J. Geophys. Res.*, *112*, D16309, doi:10.1029/2006JD008294.
- Park, M., W. J. Randel, L. K. Emmons, P. F. Bernath, K. A. Walker, and C. D. Boone (2008), Chemical isolation in the Asian monsoon anticyclone observed in Atmospheric Chemistry Experiment (ACE-FTS) data, *Atmos. Chem. Phys.*, *8*, 757–764.
- Park, M., W. J. Randel, L. K. Emmons, and N. J. Livesey (2009), Transport pathways of carbon monoxide in the Asian summer monsoon diagnosed

- from Model of Ozone and Related Tracers (MOZART), *J. Geophys. Res.*, *114*, D08303, doi:10.1029/2008JD010621.
- Penkett, S. A., R. G. Derwent, P. Fabian, R. Borchers, and U. Schmidt (1980), Methyl chloride in the stratosphere, *Nature*, *283*, 58–60.
- Pickering, K. E., et al. (1996), Convective transport of biomass burning emissions over Brazil during TRACE-A, *J. Geophys. Res.*, *101*, 23,993–24,012.
- Pierotti, D., R. A. Rasmussen, and R. Dalluge (1980), Measurements of N₂O, CF₂Cl₂, CFC₁₃, CH₃CCl₃, CCl₄, and CH₃Cl in the troposphere and lower stratosphere over North America, *J. Geomag. Geoelectr.*, *32*, 181–205.
- Ploeger, F., P. Konopka, R. Müller, S. Fueglistaler, T. Schmidt, J. C. Manners, J.-U. Grooß, G. Günther, P. M. Forster, and M. Riese (2012), Horizontal transport affecting trace gas seasonality in the tropical tropopause layer (TTL), *J. Geophys. Res.*, *117*, D09303, doi:10.1029/2011JD017267.
- Pommrich, R., R. Mueller, J. U. Grooss, G. Gunther, P. Konopka, M. Riese, A. Heil, M. Schultz, H. C. Pumphrey, and K. A. Walker (2010), What causes the irregular cycle of the atmospheric tape recorder signal in HCN?, *Geophys. Res. Lett.*, *37*, L16805, doi:10.1029/2010GL044056.
- Pumphrey, H. C., C. Boone, K. A. Walker, P. Bernath, and N. J. Livesey (2008), Tropical tape recorder observed in HCN, *Geophys. Res. Lett.*, *35*, L05801, doi:10.1029/2007GL032137.
- Pumphrey, H. C., M. L. Santee, N. J. Livesey, M. J. Schwartz, and W. G. Read (2011), Microwave Limb Sounder observations of biomass-burning products from the Australian bush fires of February 2009, *Atmos. Chem. Phys.*, *11*, 6285–6296.
- Pumphrey, H. C., et al. (2007), Validation of middle-atmosphere carbon monoxide retrievals from MLS on Aura, *J. Geophys. Res.*, *112*, D24S38, doi:10.1029/2007JD008723.
- Randel, W. J., M. Park, F. Wu, and N. Livesey (2007), A large annual cycle in ozone above the tropical tropopause linked to the Brewer-Dobson circulation, *J. Atmos. Sci.*, *64*, 4479–4488.
- Randel, W. J., M. Park, L. Emmons, D. Kinnison, P. Bernath, K. A. Walker, C. Boone, and H. Pumphrey (2010), Asian monsoon transport of pollution to the stratosphere, *Science*, *328*, 611–613.
- Rasmussen, R. A., L. E. Rasmussen, M. A. K. Khalil, and R. W. Dalluge (1980), Concentration distribution of methyl chloride in the atmosphere, *J. Geophys. Res.*, *85*, 7350–7356.
- Read, W. G., et al. (2007), Aura Microwave Limb Sounder upper tropospheric and lower stratospheric H₂O and relative humidity with respect to ice validation, *J. Geophys. Res.*, *112*, D24S35, doi:10.1029/2007JD008752.
- Redeker, K. R., and R. J. Cicerone (2004), Environmental controls over methyl halide emissions from rice paddies, *Global Biogeochem. Cycles*, *18*, GB1027, doi:10.1029/2003GB002092.
- Redeker, K. R., N.-Y. Wang, J. C. Low, A. McMillan, S. C. Tyler, and R. J. Cicerone (2000), Emissions of methyl halides and methane from rice paddies, *Science*, *290*, 966–969.
- Reid, J. S., P. Xian, E. J. Hyer, M. K. Flatau, E. M. Ramirez, F. J. Turk, C. R. Sampson, C. Zhang, E. M. Fukada, and E. D. Maloney (2012), Multi-scale meteorological conceptual analysis of observed active fire hotspot activity and smoke optical depth in the Maritime Continent, *Atmos. Chem. Phys.*, *12*, 2117–2147.
- Rhew, R., and O. Mazéas (2010), Gross production exceeds gross consumption of methyl halides in northern California salt marshes, *Geophys. Res. Lett.*, *37*, L18813, doi:10.1029/2010GL044341.
- Rhew, R. C., B. R. Miller, and R. F. Weiss (2000), Natural methyl bromide and methyl chloride emissions from coastal salt marshes, *Nature*, *403*, 292–295.
- Rhew, R. C., B. R. Miller, M. K. Vollmer, and R. F. Weiss (2001), Shrubland fluxes of methyl bromide and methyl chloride, *J. Geophys. Res.*, *106*, 20,875–20,882.
- Rhew, R. C., M. Aydin, and E. S. Saltzman (2003), Measuring terrestrial fluxes of methyl chloride and methyl bromide using a stable isotope tracer technique, *Geophys. Res. Lett.*, *30*, 2103, doi:10.1029/2003GL018160.
- Rhew, R. C., Y. A. Teh, and T. Abel (2007), Methyl halide and methane fluxes in the northern Alaskan coastal tundra, *J. Geophys. Res.*, *112*, G02009, doi:10.1029/2006JG000314.
- Ricaud, P., et al. (2007), Impact of land convection on troposphere-stratosphere exchange in the tropics, *Atmos. Chem. Phys.*, *7*, 5639–5657.
- Rienecker, M. M., et al. (2008), The GEOS-5 data assimilation system—Documentation of Versions 5.0.1 and 5.1.0, NASA Goddard Space Flight Center, Greenbelt, Maryland.
- Rienecker, M. M., et al. (2011), MERRA—NASA’s Modern-Era Retrospective Analysis for Research and Applications, *J. Climate*, *24*, 3624–3648, doi:10.1175/JCLI-D-11-00015.1.
- Rinsland, C. P., G. Dufour, C. D. Boone, P. F. Bernath, L. Chiou, P.-F. Coheur, S. Turquety, and C. Clerbaux (2007), Satellite boreal measurements over Alaska and Canada during June–July 2004: Simultaneous measurements of upper tropospheric CO, C₂H₆, HCN, CH₃Cl, CH₄, C₂H₂, CH₃OH, HCOOH, OCS, and SF₆ mixing ratios, *Global Biogeochem. Cycles*, *21*, GB3008, doi:10.1029/2006GB002795.
- Rodgers, C. D. (2000), *Inverse Methods for Atmospheric Sounding: Theory and Practice*, World Sci., Singapore.
- Saito, T., Y. Yokouchi, Y. Kosugi, M. Tani, E. Philip, and T. Okuda (2008), Methyl chloride and isoprene emissions from tropical rain forest in Southeast Asia, *Geophys. Res. Lett.*, *35*, L19812, doi:10.1029/2008GL035241.
- Santee, M. L., G. L. Manney, N. J. Livesey, and W. G. Read (2004), Three-dimensional structure and evolution of stratospheric HNO₃ based on UARS Microwave Limb Sounder measurements, *J. Geophys. Res.*, *109*, D15306, doi:10.1029/2004JD004578.
- Santee, M. L., G. L. Manney, N. J. Livesey, L. Froidevaux, M. J. Schwartz, and W. G. Read (2011), Trace gas evolution in the lowermost stratosphere from Aura Microwave Limb Sounder measurements, *J. Geophys. Res.*, *116*, D18306, doi:10.1029/2011JD015590.
- Santee, M. L., et al. (2007), Validation of the Aura Microwave Limb Sounder HNO₃ measurements, *J. Geophys. Res.*, *112*, D24S40, doi:10.1029/2007JD008721.
- Santee, M. L., et al. (2008), Validation of the Aura Microwave Limb Sounder ClO measurements, *J. Geophys. Res.*, *113*, D15S22, doi:10.1029/2007JD008762.
- Schauffler, S. M., L. E. Heidt, W. H. Pollock, T. M. Gilpin, J. F. Vedder, S. Solomon, R. A. Lueb, and E. L. Atlas (1993), Measurements of halogenated organic compounds near the tropical tropopause, *Geophys. Res. Lett.*, *20*, 2567–2570.
- Schauffler, S. M., et al. (2003), Chlorine budget and partitioning during the Stratospheric Aerosol and Gas Experiment (SAGE) III Ozone Loss and Validation Experiment (SOLVE), *J. Geophys. Res.*, *108*(D5), 4173, doi:10.1029/2001JD002040.
- Scheeren, H. A., J. Lelieveld, J. A. de Gouw, C. van der Veen, and H. Fischer (2002), Methyl chloride and other chlorocarbons in polluted air during INDOEX, *J. Geophys. Res.*, *107*(D19), 8015, doi:10.1029/2001JD001121.
- Scheeren, H. A., et al. (2003), The impact of monsoon outflow from India and Southeast Asia in the upper troposphere over the eastern Mediterranean, *Atmos. Chem. Phys.*, *3*, 1589–1608.
- Schmidt, U., D. Knapska, and S. A. Penkett (1985), A study of the vertical distribution of methyl chloride (CH₃Cl) in the midlatitude stratosphere, *J. Atmos. Chem.*, *3*, 363–376.
- Schoeberl, M. R., B. N. Duncan, A. R. Douglass, J. Waters, N. Livesey, W. Read, and M. Filipiak (2006), The carbon monoxide tape recorder, *Geophys. Res. Lett.*, *33*, L12811, doi:10.1029/2006GL026178.
- Schoeberl, M. R., et al. (2008), QBO and annual cycle variations in tropical lower stratosphere trace gases from HALOE and Aura MLS observations, *J. Geophys. Res.*, *113*, D05301, doi:10.1029/2007JD008678.
- Scholze, M., W. Knorr, N. W. Arnell, and I. C. Prentice (2006), A climate-change risk analysis for world ecosystems, *Proc. Natl. Acad. Sci. U.S.A.*, *103*, 13,116–13,120.
- Schultz, M. G., A. Heil, J. J. Hoelzemann, A. Spessa, K. Thonicke, J. G. Goldammer, A. C. Held, J. M. C. Pereira, and M. van het Bolscher (2008), Global wildland fire emissions from 1960 to 2000, *Global Biogeochem. Cycles*, *22*, GB2002, doi:10.1029/2007GB003031.
- Scott, R. K., E. F. Shuckburgh, J.-P. Cammas, and B. Legras (2003), Stretching rates and equivalent length near the tropopause, *J. Geophys. Res.*, *108*(D13), 4394, doi:10.1029/2002JD002988.
- Sen, B., et al. (1999), The budget and partitioning of stratospheric chlorine during the 1997 Arctic summer, *J. Geophys. Res.*, *104*, 26,653–26,665.
- Shuckburgh, E., W. Norton, A. Iwi, and P. Haynes (2001), Influence of the quasi-biennial oscillation on isentropic transport and mixing in the tropics and subtropics, *J. Geophys. Res.*, *106*, 14,327–14,337.
- Simmonds, P. G., A. J. Manning, R. G. Derwent, P. Ciais, M. Ramonet, V. Kazan, and D. Ryall (2005), A burning question: Can recent growth rate anomalies in the greenhouse gases be attributed to large-scale biomass burning events?, *Atmos. Env.*, *39*, 2513–2517.
- Simmonds, P. G., et al. (2004), AGAGE observations of methyl bromide and methyl chloride at Mace Head, Ireland, and Cape Grim, Tasmania, 1998–2001, *J. Atmos. Chem.*, *47*, 243–269.
- Singh, H. B., L. J. Salas, and R. E. Stiles (1983), Methyl halides in and over the Eastern Pacific (40°N–32°S), *J. Geophys. Res.*, *88*, 3684–3690.
- Singh, H. B., et al. (2003), In situ measurements of HCN and CH₃CN over the Pacific Ocean: Sources, sinks, and budgets, *J. Geophys. Res.*, *108*, 8795, doi:10.1029/2002JD003006.
- Symonds, R. B., W. I. Rose, and M. H. Reed (1988), Contribution of Cl- and F-bearing gases to the atmosphere by volcanoes, *Nature*, *334*, 415–418.

- Tait, V. K., R. M. Moore, and R. Tokarczyk (1994), Measurements of methyl chloride in the northwest Atlantic, *J. Geophys. Res.*, *99*, 7821–7833.
- Tokarczyk, R., E. S. Saltzman, R. M. Moore, and S. A. Yvon-Lewis (2003a), Biological degradation of methyl chloride in coastal seawater, *Global Biogeochem. Cycles*, *17*(2), 1057, doi:10.1029/2002GB001949.
- Tokarczyk, R., K. D. Goodwin, and E. S. Saltzman (2003b), Methyl chloride and methyl bromide degradation in the Southern Ocean, *Geophys. Res. Lett.*, *30*(15), 1808, doi:10.1029/2003GL017459.
- Toohey, M., and T. von Clarmann (2013), Climatologies from satellite measurements: The impact of orbital sampling on the standard error of the mean, *Atmos. Meas. Tech.*, *6*, 937–948.
- Toon, G. C. (1991), The JPL MkIV interferometer, *Opt. Photon. News*, *2*, 19–21.
- Toon, G. C., et al. (1999), Comparison of MkIV balloon and ER-2 aircraft measurements of atmospheric trace gases, *J. Geophys. Res.*, *104*, 26,779–26,790.
- Trudinger, C. M., D. M. Etheridge, G. A. Sturrock, P. J. Fraser, P. B. Krummel, and A. McCulloch (2004), Atmospheric histories of halocarbons from analysis of Antarctic firn air: Methyl bromide, methyl chloride, chloroform, and dichloromethane, *J. Geophys. Res.*, *109*, D22310, doi:10.1029/2004JD004932.
- van der Werf, G. R., et al. (2010), Global fire emissions and the contribution of deforestation, savanna, forest, agricultural, and peat fires (1997–2009), *Atmos. Chem. Phys.*, *10*, 11,707–11,735.
- Varner, R. K., P. M. Crill, and R. W. Talbot (1999), Wetlands: A potentially significant source of atmospheric methyl bromide and methyl chloride, *Geophys. Res. Lett.*, *26*, 2433–2436.
- Velazco, V. A., G. C. Toon, J.-F. Blavier, A. Kleinböhl, G. L. Manney, W. H. Daffer, P. F. Bernath, K. A. Walker, and C. Boone (2011), Validation of the Atmospheric Chemistry Experiment by noncoincident MkIV balloon profiles, *J. Geophys. Res.*, *116*, D06306, doi:10.1029/2010JD014928.
- Waters, J. W., et al. (2006), The Earth Observing System Microwave Limb Sounder (EOS MLS) on the Aura satellite, *IEEE Trans. Geosci. Remote Sens.*, *44*, 1075–1092.
- Watling, R., and D. B. Harper (1998), Chloromethane production by wood-rotting fungi and an estimate of the global flux to the atmosphere, *Mycol. Res.*, *102*, 769–787.
- Weisenstein, D. K., M. K. W. Ko, and N.-D. Sze (1992), The chlorine budget of the present-day atmosphere: A modeling study, *J. Geophys. Res.*, *97*, 2547–2559.
- Westerling, A. L., H. G. Hidalgo, D. R. Cayan, and T. W. Swetnam (2006), Warming and earlier spring increase western U.S. forest wildfire activity, *Science*, *313*, 940–943.
- Widayati, A., H. L. Tata, S. Rahayu, and Z. Said (2012), *Conversions of Tripa peatswamp forest and the consequences on the loss of Sumatran Orangutan (Pongo abelii) habitat and on aboveground CO₂ emissions*, *Tripa Series 33*, World Agroforestry Centre (ICRAF), Southeast Asia Regional Program, Bogor, Indonesia.
- Williams, M. B., M. Aydin, C. Tatum, and E. S. Saltzman (2007), A 2000 year atmospheric history of methyl chloride from a South Pole ice core: Evidence for climate-controlled variability, *Geophys. Res. Lett.*, *34*, L07811, doi:10.1029/2006GL029142.
- World Meteorological Organization (2007), *Scientific Assessment of Ozone Depletion: 2006*, Global Ozone Res. and Monit. Proj. Rep. 50, Geneva, Switzerland.
- World Meteorological Organization (2011), *Scientific Assessment of Ozone Depletion: 2010*, Global Ozone Res. and Monit. Proj. Rep. 52, Geneva, Switzerland.
- Xiao, X., et al. (2010), Optimal estimation of the surface fluxes of methyl chloride using a 3-D global chemical transport model, *Atmos. Chem. Phys.*, *10*, 5515–5533.
- Yokouchi, Y., M. Ikeda, Y. Inuzuka, and T. Yukawa (2002), Strong emission of methyl chloride from tropical plants, *Nature*, *416*, 163–165.
- Yokouchi, Y., et al. (2000), A strong source of methyl chloride to the atmosphere from tropical coastal land, *Nature*, *403*, 295–298.
- Yoshida, Y., Y. Wang, T. Zeng, and R. Yantosca (2004), A three-dimensional global model study of atmospheric methyl chloride budget and distributions, *J. Geophys. Res.*, *109*, D24309, doi:10.1029/2004JD004951.
- Yoshida, Y., Y. Wang, C. Shim, D. Cunnold, D. R. Blake, and G. S. Dutton (2006), Inverse modeling of the global methyl chloride sources, *J. Geophys. Res.*, *111*, D16307, doi:10.1029/2005JD006696.
- Yvon-Lewis, S. A., D. B. King, R. Tokarczyk, K. D. Goodwin, E. S. Saltzman, and J. H. Butler (2004), Methyl bromide and methyl chloride in the Southern Ocean, *J. Geophys. Res.*, *109*, C02008, doi:10.1029/2003JC001809.
- Zander, R., M. R. Gunson, C. B. Farmer, C. P. Rinsland, F. W. Irion, and E. Mahieu (1992), The 1985 chlorine and fluorine inventories in the stratosphere based on ATMOS observations at 30° north latitude, *J. Atmos. Chem.*, *15*, 171–186.
- Zander, R., et al. (1996), The 1994 northern midlatitude budget of stratospheric chlorine derived from ATMOS/ATLAS-3 observations, *Geophys. Res. Lett.*, *23*, 2357–2360.